Paper II

Dismembering of subducted continental crust by nappe stacking during continental collision: an example from the Reisa Nappe Complex in the Scandinavian Caledonides, northern Norway

Carly Faber[1], Holger Stünitz[1], Deta Gasser[2,3], Petr Jeřábek[4], Katrin Kraus[1], Fernando Corfu[5], Erling Krogh Ravna[1]; Jiří Konopásek[1]

[1]Department of Geosciences, UiT The Arctic University of Norway, Tromsø, N-9037, Norway
[2]Western Norway University of Applied Sciences, Sogndal 6851, Norway
[3]Geological Survey of Norway, Trondheim 7491, Norway
[4]IPSG, Faculty of Science, Charles University, Albertov 6, 128 43, Prague 2, Czech Republic
[5]Department of Geosciences & Centre for Earth Evolution and Dynamics, University of Oslo, Norway

*corresponding author (e-mail: carlyfaber1@gmail.com)

Abstract

This study investigates the Caledonian metamorphic evolution in northern Norway, examining the structure of the Reisa Nappe Complex (RNC) and timing and P-T conditions of deformation and metamorphism that formed nappes , facilitating crustal thickening during continental collision. The study describes the extent and tectonostratigraphy of the RNC (from bottom to top, Vaddas, Kåfjord and Nordmannvik Nappes) east of Lyngen and uses phase equilibrium modelling and U-Pb zircon and titanite geochronology to describe the tectonometamorphic evolution of the RNC. Phase equilibrium modelling for five samples taken from different parts of the RNC reveals an anticlockwise Caledonian P-T path attributed to the effect of an early Silurian heating event followed by burial and Caledonian thrusting. An early Caledonian S1 foliation in the Nordmannvik Nappe records kyanite-grade partial melting at ~760 – 790 °C and ~9.4 – 11 kbar. Conditions associated with this early event in the lower Kåfjord Nappe are at lower P-T (590 – 625 °C and 5.9-6.9 kbar), indicating a higher relative position in the crust. A basal comglomerate in the underlying Vaddas Nappe suggests the Vaddas and lower Kåfjord metasediments were probably deposited on a KNC basement, and likely rapidly buried. Leucosome in Caledonian fold axial planes in the Nordmannvik Nappe rocks indicates that initial Caledonian compressional deformation initiated while the rocks were still partially molten. Melt crystallized at 439 ± 2 Ma (U-Pb zircon), and Caledonian solid state shearing followed as the rocks cooled and solidified. S2 foliation

P-T conditions in the Nordmannvik Nappe are estimated at 680 – 730 °C and 9.5 – 10.9 kbar. Long-lived titanite growth in the Nordmannvik Nappe records this extended metamorphism between 444 and 427 Ma. Gabbro intrusion into the Vaddas Nappe occurred at 439 ± 1 Ma, synchronous with migmatization in the Nordmannvik Nappe. Caledonian S2 shearing in the Vaddas and lower Kåfjord Nappes is between ~600 – 690 °C and 9.8 – 12.3 kbar, with the higher pressure estimates in the Vaddas. Syn-S2 titanite growth along the lower RNC boundary records shearing at 432 ± 6 Ma. Based on the current tectonostratigraphy a block model is constructed for the relative paleogeography of the pre-Caledonian Baltica margin. The anticlockwise P-T path can be explained best either by: 1) heating in an incipient back arc prior to continental collision, or 2) slab breakoff during initial continental collision. Migmatization in the fertile subducted Nordmannvik Nappe rocks, which formed part of the pre-Caledonian extended Baltica margin prior to collision, caused strain localization and probably facilitated the initiation of nappe stacking, inhibiting deep subduction of the RNC rocks.

1. Introduction

Continental collision is a fundamental process that profoundly reshapes crustal rocks and facilitates the building of new continental crust by bringing a variety of terranes together. Large-scale thrusting and nappe stacking are the main processes responsible for crustal shortening during continental collision. Depending on their rheology crustal rocks can be subducted to depths of ~200 km (e.g. Chopin, 2003; Spengler et al., 2009; Hacker et al., 2010), or be included in large-scale ductile nappe stacks (e.g. Escher et al., 1993; Escher and Beaumont, 1997). Crucial factors that control the style of large-scale deformation and mid- to lower crustal ductile nappe stacking are temperature, availability of fluids, composition of the rocks involved, and the presence or absence of melt that either stabilize or weaken the subducting blocks (e.g. Hollister and Crawford, 1986; Beaumont et al., 2006; Gerya and Meilick, 2010; Labrousse et al., 2010; Jeřábek et al., 2012). Metamorphic reactions at depth crucially influence several of these controlling factors, and the interplay between magmatic, metamorphic and deformational processes determines the final style of crustal shortening and nappe stacking. In active continental collision zones such as the Himalaya, mid- and lower-crustal processes are generally

inferred from surface deformation, geophysical information, and the geochemistry of erupted volcanic rocks (e.g. Schulte-Pelkum et al., 2005; Zhao et al., 2009). In contrast, ancient and deeply eroded continental collision zones allow for direct study of nappe stacks formed at mid- and lower crustal levels, allowing important insights into the processes leading to large-scale continental subduction and crustal shortening.

The Caledonian orogen was formed by convergence and collision between Baltica and Laurentia in the Silurian-Devonian (Fig. 1A). The resulting large-scale nappe stacks provide access to the study of mid- to lower-crustal processes during a continental collision of Himalayan style and extent (e.g. Streule et al., 2010; Labrousse et al., 2010). In northern Norway, a complete section from the autochthonous Baltican basement to exotic ophiolitic nappes is exposed (Fig. 1B), displaying large gradients in metamorphic grade and deformational style (Corfu et al., 2014). The Reisa Nappe Complex (RNC) represents a large ductile nappe stack, metamorphosed at amphibolite- to granulite-facies conditions, displaying pervasive ductile deformation and possible Caledonian partial melting (Roberts and Sturt, 1980; Andresen, 1988). Its current tectonostratigraphic position directly below the only oceanic rocks in the region (the Lyngsfjellet Nappe) suggests it may have been at the Baltica continental edge prior to continental collision. Mechanical weakening caused by Caledonian partial melting of the rocks may have significantly affected the style of continental collision. Understanding the structure and composition of the RNC together with its metamorphic, deformation, and magmatic history will help to establish how its pre-Caledonian and Caledonian evolution affected deformation behavior and lower crustal nappe stacking during continental collision in this particular part of the Caledonian Orogen.

2. Geological Framework

The Scandinavian Caledonides consist of a series of allochtonous nappes, showing from bottom to top Baltican, Iapetus, or Laurentian affinities (Roberts and Gee, 1985; Stephens & Gee, 1989; Fig. 1A).

2.1. The North Norwegian Caledonides

In northern Norway a complete section through the Caledonian nappe stack is exposed (Fig. 1B; e.g. Ramsay et al., 1985). The Baltican basement with its metasedimentary autochthonous cover is overlain by the parautochthonous metasedimentary rocks of the Gaissa Nappe Complex. The allochtonous rocks form a nappe stack including the following units, from bottom to top: 1) the metasedimentary and metaigneous rocks of the Kalak Nappe Complex (KNC), 2) the metasedimentary and metaigneous rocks of the Reisa Nappe Complex (RNC), 3) the ophiolitic and metasedimentary rocks of the Lyngsfjellet Nappe Complex (LNC), 4) gneisses and migmatites of the Nakkedalen Nappe, 4) and metasediments of the Tromsø Nappe (Andresen, 1988; Kvassnes et al., 2004; Kirkland et al., 2006, 2007a Augland et al., 2014; Rice, 2014; Gee et al., 2017). Caledonian metamorphic conditions associated with nappe thrusting generally increase upwards through the KNC and RNC, from low greenschist facies in parautochtonous metasediments to upper amphibolite/lower granulite facies at the top of the RNC, with local granulite facies generally interpreted to be pre-Caledonian (Andresen, 1988; Elvevold et al., 1993, 1994;). The LNC displays greenschist facies metamorphism at its base with higher-grade metamorphism in the overlying metasediments, and the overlying Nakkedalen and Tromsø nappes show amphibolite to eclogite facies metamorphism (Andresen and Bergh, 1985; Andresen & Steltenpohl, 1994; Corfu et al., 2003). The main Caledonian deformation (often referred to as Scandian; e.g. Corfu et al., 2014) in the allochthons in northern Norway is associated with top-to-SE and top-to-E shear sense (Rice, 1998). The KNC and RNC display mainly pervasive Caledonian deformation, but older deformational phases are preserved locally (e.g. Gasser et al., 2015).

The palaeogeographic origin of several of the Caledonian nappe stacks in northern Norway is debated. The Gaissa Nappe Complex is interpreted to represent telescoped Baltican margin cover, and the KNC has traditionally also been interpreted to represent more outboard Baltican basement and its late Precambrian to Paleozoic cover (e.g. Stephens and Gee, 1989; Gee et al., 2017). However, recent new evidence shows that the sedimentary cover had actually been deposited already between 1000 and 900 Ma, and underwent metamorphism, deformation and magmatism during several events at about

970-950 Ma, 870-830 Ma, 700 Ma, 600 Ma and 570 Ma. These Neoproterozoic events are not known in the Baltic basement elsewhere implying that either the KNC has an exotic origin, or that a still unknown type of suture (typical suture rocks are lacking beneath the KNC) separated it from the Archean – Palaeoproterozoic northern Baltic basement before the final collision (e.g. Kirkland et al., 2006, 2007a, 2007, 2008; Corfu et al., 2007, 2011). The RNC has previously been interpreted to represent either Iapetus-derived or outermost Baltican rocks, whereas the Lyngsfjellet Nappe is traditionally considered as Iapetus-derived, marking the transition towards the Laurentia-derived Nakkedalen and Tromsø Nappes (e.g. Stephens and Gee, 1989; Corfu et al., 2003).

2.2. The Reisa Nappe Complex

The RNC outcrops east of Lyngen (Fig. 1B) and includes, from bottom to top, the Vaddas, Kåfjord and Nordmannvik Nappes (Figs. 1, 2; Zwaan & Roberts, 1978; Zwaan, 1988). The Vaddas Nappe has been best studied in the southeastern part of our study area and has been divided into a lower and upper part (Fig. 3; Lindahl et al., 2005). The lower part is mapped only in between Straumfjord and Kvænangen and includes a basal marble and calc-silicate layer, garnet- and graphite-bearing schist, meta-arkose, quartzite and amphibolite, representing metamorphosed volcanosedimentary rocks and turbidites (Andresen, 1988; Lindahl et al., 2005). The 602 ± 5 Ma Rappesvarre metagranite occurs in the lower part of the nappe, although its relationship with the surrounding rocks is unclear. It may represent a thrust slice of the KNC below (Figs. 2, 3; Lindahl et al., 2005; Corfu et al., 2007; Gee et al., 2017).

The base of the upper part of the Vaddas Nappe includes a quartzite-conglomerate and marble layer with local late Ordovician-early Silurian fossils (447-441 Ma; Fig. 3; Binns and Gayer, 1980). Above, garnet-bearing calc-schist with layers and lenses of amphibolite underlie a thick sequence of metapsammites (Zwaan, 1988; Lindahl et al., 2005). Several undated tholeiitic gabbro bodies intrude the upper Vaddas rocks (Kågen, Kvænangen and Vaddas gabbros, Figs. 2, 3; Lindahl et al., 2005). The Halti Igneous Complex (Fig. 1B), either a klippe of the Vaddas Nappe (Vaasjoki and Sipilä, 2001) or an intrusion in the KNC (Andréasson et al., 2003), yields intrusion ages of 434 ± 5 Ma and

438 ± 5 Ma. The Magerøy Nappe and Hellefjord schists in the northeast and Køli Nappe in the southwest are thought to be equivalents of the Vaddas Nappe (Fig. 1B; Gayer & Roberts, 1973; Lindahl et al., 2005; Corfu et al., 2006, 2011; Kirkland et al., 2005, 2016). Volcaniclastic and intrusive rocks in the Magerøy Nappe give early Silurian ages (442-435 Ma) suggesting almost synchronous deposition and intrusion (Robins, 1998; Corfu et al., 2011; Kirkland et al., 2005, 2016).

Both the Vaddas and Kåfjord nappes display amphibolite facies metamorphic conditions and pervasive shearing. They are separated by a strongly mylonitic zone (Zwaan and Roberts, 1978; Andresen, 1988; Zwaan, 1988). The lower part of the Kåfjord Nappe is composed of marble and calc-schist, metapsammite and garnet micaschist. Mylonitic gneisses with boudinaged amphibolite and granitic bodies dominate the upper part of the nappe (Andresen, 1988). Small gabbro bodies of unknown age also occur (Zwaan, 1988). A Rb-Sr whole-rock age suggests anatexis and granite crystallization at 440 Ma in the upper part of the nappe (Dangla et al., 1978). The boundary between the Kåfjord and the overlying Nordmannvik nappe is a well-developed mylonitic zone (Andresen, 1988).

The Nordmannvik Nappe, defined east of Lyngen at Nordmannvik and best studied from Nordmannvik to Heia (Fig. 1B) is a polymetamorphic nappe showing a pervasive amphibolite facies foliation surrounding granulite facies relict lenses. Mineral grains also record relict granulite facies conditions (Elvevold, 1987; Andresen, 1988; Zwaan, 1988; Lindstrøm and Andresen, 1992; Augland et al., 2014). The nappe is comprised of garnet-mica schist and gneiss, migmatite, minor calc-silicate, amphibolite, and marble (Fig. 3). Small bodies of gabbro and sagvandite (metasomatic carbonate-orthopyroxenite) occur within the nappe (Schreyer et al., 1972; Lindstrøm and Andresen, 1992). Metamorphic conditions at Heia (Fig. 1B) were estimated at 715 ± 30 °C and 9.2 ± 1 kbar using multiple geothermometers and geobarometers (Elvevold, 1987). U-Pb zircon ages from the Heia gabbro indicate high-temperature metamorphism at 439 ± 1 Ma and gabbro crystallization at 435 ± 1 Ma, overprinted by Caledonian shearing at 420 ± 4 Ma (Augland et al., 2014). The upper part of the Narvik Nappe Complex farther to the southwest (Fig. 1A, NNC) may be an equivalent of the Nordmannvik Nappe (Binns,

1978; Steltenpohl et al., 1990; Tucker et al., 1990; Augland et al., 2014). Greenschist facies mylonitic rocks mark the boundary between the Nordmannvik Nappe and Lyngsfjellet Nappe above. The Lyngsfjellet Nappe is comprised of greenschist to amphibolite facies fossiliferous metasedimentary rocks unconformably overlying the mafic-ultramafic Lyngen Magmatic Complex, interpreted as an ophiolite formed in an incipient arc setting (possible Laurentian arc; Figs. 1, 3; Zwaan, 1988; Stephens and Gee, 1989; Andresen & Bergh, 1985; Andresen and Steltenpohl, 1994; Kvassnes et al., 2004). Timing and kinematics of emplacement of the Lyngsfjellet Nappe over the Nordmannvik Nappe are unclear.

3. Tectonostratigraphy and large-scale structure of the RNC

We investigated the RNC east and north of Lyngen in coastal areas, where it is exposed around a window of KNC rocks (Figs. 1, 2). A detailed structural section through the RNC was investigated on Uløya, supplemented by structural mapping along the east coast of Lyngen, on Kågen and around Straumfjord (Figs. 2, 3). In addition, a detailed structural section was investigated through the nappe stack on Arnøya. The nappes on Arnøya were previously assigned entirely to the KNC (Roberts, 1973; Zwaan, 1988), but reconsidered as being part of the Vaddas Terrane (Andresen, 1988). More recent maps have classified northern Arnøya as part of the Magerøy/Vaddas Nappe and southern Arnøya as KNC (e.g. Corfu et al., 2007; Augland et al., 2014; Gasser et al., 2015). Our preliminary field observations indicated a correlation of the upper nappes on Arnøya with the RNC, confirmed during further detailed fieldwork (e.g. Figs. 1B, 2).

3.1 Field observations

The lower boundary of the RNC towards the KNC was investigated on Uløya and Arnøya (Fig. 2). The underlying KNC comprises either quartzofeldspathic rocks or metapelitic paragneisses (Fig. 4A), whereas the boundary itself consists of a ~40 m-thick strongly mylonitic zone comprised of intercalated amphibolite-facies quartzofeldspathic rocks, gneisses and schists. Marbles are locally present together with the amphibolite and schist. On Uløya a migmatitic paragneiss that forms part of the KNC side of the boundary is mylonitized and garnet and feldspar form cm-sized porphyroclasts (Fig. 4B, C).

Kinematic indicators consistently show top-to-SE shearing. Above the mylonitic layer, there is sheared metaconglomerate (Fig. 4D) both on Uløya and Arnøya. It is sheared together with a marble unit. This layer often marks the base of the Vaddas Nappe. It is overlain by metavolcanic rocks and calc-schist (Fig. 4E). The metavolcanic rocks and calc-schists also occur on Kågen (Fig. 3). In contrast, around Straumfjord two main marble units and also minor marble layers occur in the metasediments of the Vaddas Nappe (Fig. 3). The lowermost variably sheared marble marks the base of the lower Vaddas and is overlain by intercalated metasediments and metapsammites more similar to those in the KNC. The uppermost marble layer marks the base of the upper Vaddas and is associated with sheared conglomerates. It is overlain by metavolcanics and calc-schists, similarly to the Vaddas succession on Arnøya, Kågen and Uløya (Fig. 3). On Arnøya, Kågen and in Straumfjord, gabbro intrusions (Figs. 2, 3) are associated with local migmatisation of the surrounding metasediments, showing a clear intrusive relationship.

A well-developed strongly mylonitic foliation in muscovite-rich garnet-mica-schist marks the Vaddas-Kåfjord nappe boundary on Uløya and Arnøya (Figs. 2, 3). The boundary cuts the gabbro in its lower part on Arnøya (Fig. 3). The Kåfjord Nappe is comprised of a lower unit of fairly homogenous garnet-mica-zoisite schist with calc-silicate lenses and some amphibolite layers (Fig. 4G-I), and a fairly homogenous upper unit comprised of garnet-mica-schist and gneiss. This upper unit often displays strongly sheared layers rich in sheared quartz-feldspar sigma clasts, possibly indicating the presence of leucosome prior to mylonitization. The lower Kåfjord is similar to calc-schists in the underlying Vaddas Nappe, whereas the upper Kåfjord is similar to strongly sheared rocks in the Nordmannvik nappe (e.g Figs. 3, 5A). Both units are pervasively and strongly sheared at amphibolite facies conditions. The current Kåfjord - Nordmannvik boundary consists of mylonitic gneisses and garnet-mica-schist at least 50 m-thick. The Nordmannvik Nappe is mainly comprised of garnet-biotite-gneiss with layers and lenses of amphibolite and local calc-silicates, generally dominated by a mylonitic foliation (Fig. 5A). Further away from the nappe boundary rare relict lenses (< 50 m) display a higher-grade migmatitic foliation (e.g. Fig. 5C). Although the nappe is pervasively sheared, on Arnøya the

frequency of relict lenses increases upwards away from the nappe boundary. The migmatite comprises felsic leucosome and biotite, garnet and kyanite in the restite. The amount of leucosome varies spatially between 5-25% (Figs. 5D, E). Layers of amphibolite in the nappe also contain minor tonalitic leucosome suggesting that the mafic rocks have also been migmatised.

3.2 Structures in the RNC

The syn-migmatitic foliation (S1: Fig. 2A, E) is observed in low strain lens-shaped domains in the Nordmannvik Nappe (Fig. 5C). It is typically present in domains further away from the nappe boundaries. This foliation represents the earliest observed structural element (S1). In most cases it is sheared and overprinted by the solid-state amphibolite-facies mylonitic foliation, the S2 foliation, which is pervasive throughout all the nappes of the RNC and KNC (Fig. 2A-F). In the lower strain lenses the S1 migmatitic foliation is found in 3 structural orientations: 1) as a steep foliation that shows a variable trend (rare), 2) folded in open to closed folds with axial planes (containing leucosome) parallel to the S2 foliation, and 3) most commonly as a shallowly-dipping foliation, parallel to the S2 foliation (Fig. 2A, D, E). Fold hinges in the migmatites plunge towards SE or NW, parallel to the L2 lineation. A weak intersection lineation is found in the shallowly-dipping migmatites, parallel to L2 (L1; Fig 2A, D, E), and may represent the intersection between the steep and shallow orientations of the S1 migmatitic foliation. Melt segregations within S2-parallel fold axial planes indicate that the rocks were partially molten during Caledonian thrusting (Fig. 5D).

The amphibolite-facies solid-state S2 foliation is generally flat-lying, dipping slightly to the west/north-west in the northern and western areas and toward the east and southeast in the eastern areas. The main variation is around the larger gabbro bodies, when it bends around them (Fig. 2). Gabbro interiors are minimally affected by S2 shearing with the majority of deformation occurring along their boundaries. The S2 foliation is associated with a generally NW-SE-trending stretching lineation (L2; Fig. 2) and top-to-SE shear sense indicators (Fig. 4B, F, G). On Arnøya and Uløya some L2 lineations plunge shallowly towards the SSW, SW and W, falling on an apparent girdle with the NW-SE-

trending stretching lineations. These SSW, SW and W-trending lineation measurements come mainly from the upper Kåfjord and Nordmannvik nappes and mostly record intersection lineations between S1 foliation in its variable steep orientation and the shallowly-dipping S2 foliation, and some small isoclinal fold axes. In the Vaddas and Kåfjord metasediments occasional small- to meso-scale, isoclinal folds transpose an earlier fabric. Dismembered fold hinges are common, with fold axes normally parallel to L2 and fold axial planes parallel to S2 (Fig. 2A, B, D, E). The KNC-Vaddas, Vaddas-Kåfjord and Kåfjord-Nordmannvik nappe boundaries generally display a relatively stronger S2 mylonitic foliation than within the nappes, and the L2 stretching lineation at the nappe boundaries is often more pronounced than within nappe interiors.

3.3 Tectonostratigraphic interpretation

Based on our field observations and structural measurements we propose a correlation of the different parts of the RNC across the study area (Fig. 3). Lithological similarities indicate that the basal marble/conglomerate layer of the Vaddas Nappe on Arnøya, Kågen and Uløya correlates with the uppermost marble/conglomerate layer in the upper Vaddas Nappe around Straumfjord at a similar tectonostratigraphic level to where Binns and Gayer (1980) identified early Silurian fossils (Fig. 3). This indicates that the lower Vaddas rocks, which are relatively thick in the eastern study area, thin out towards the north and west and are not present elsewhere in the field area (Fig. 3). The continuation of the Kågen gabbro on southern Arnøya indicates that the Vaddas Nappe outcrops there (Figs. 2, 3). Our investigation of the Arnøya nappes shows an identical nappe stack as present on Uløya, indicating that the northwestern half of Arnøya is part of the RNC (Figs. 2, 3). The kyanite-bearing migmatites and gneisses on the northern part of Arnøya are assigned to the Nordmannvik Nappe based on their similarity to migmatites at Lyngseidet and on southern Uløya, and their tectonostratigraphic position (Fig. 3). All nappes show significant thickness variations throughout the study area: the Vaddas Nappe shows thicknesses of 100-1500 m and wedging out of its lower part towards the west and north, the Kåfjord Nappe is thickest in its southern part (>1000 m) and thins towards Arnøya (< 1000 m), whereas the Nordmannvik Nappe is significantly thicker (> 2000 m) than the Vaddas or Kåfjord nappes and thickest on Arnøya (Figs. 2, 3). This

results in laterally extensive but lensoid flat-lying thrust sheets, which are separated by mylonitic shear zones but which are internally pervasively sheared (Fig. 2, sections A`-B` and C`-D`). We separate the Kåfjord Nappe, based on lithological differences, into upper and lower parts. The upper part is similar to the strongly sheared rocks of the Nordmannvik Nappe, and records a Rb-Sr ~440 Ma age for anatexis (Dangla et al., 1978), and therefore should probably be considered as part of the Nordmannvik Nappe. The lower part is comprised of calcareous metasediments that show no evidence for prior anatexis and have more of an affinity with the underlying metasediments of the Vaddas Nappe. However, the lower boundary of these rocks cuts the upper part of the gabbro in the Vaddas Nappe on Arnøya. The lower Kåfjord therefore probably forms a thin thrust sheet of Vaddas-type metasediments.

4 Metamorphism in the RNC

Metamorphic conditions were investigated throughout the entire RNC in order to resolve variations in P-T and deformation conditions throughout the nappe stack. Sample sites and details are shown in Figure 2, 3 and Table 1. Table 2 gives a summary of the mineralogy for samples used for P-T modelling. Mineral abbreviations are according to Whitney and Evans (2010). P–T conditions for all samples were estimated using phase equilibrium modelling applied with the Perple_X software (Connolly, 2005: version 6.6.6) using the internally consistent thermodynamic data set of Holland & Powell (1998: 2004 upgrade). The calculations were performed in the MnNCKFMASHTi system using XRF whole-rock compositions (Table S1). The following solution mixing models were used: garnet, staurolite, chloritoid (Holland & Powell, 1998), biotite (Tajčmanová et al., 2009), ternary feldspar (Fuhrman & Lindsley, 1988), ilmenite (ideal mixing of ilmenite, geikielite, and pyrophanite end-members), melt (Holland & Powell, 2001) and white mica (Coggon & Holland, 2002). Iron was assumed to be Fe^{2+} as the Fe^{3+} content of the minerals considered is negligible and Fe^{3+} oxides occur in negligible amounts. Apatite was observed in all samples and therefore the corresponding amount of CaO bonded to P_2O_5 observed in the whole rock analyses was subtracted from the bulk compositions. Measured chemical compositions of the relevant minerals (Tables 3 and 4) were compared with model isopleths in the calculated pseudosections. Molar percent of

grossular (Grs) and spessartine (Sps) end-members and the X_{Mg} (Mg/Mg + Fe_{tot}) value in garnet are used to constrain P-T conditions, and are shown on the P-T sections. Estimated P-T conditions were checked with anorthite content in plagioclase (An = Ca/Ca + Na + K), X_{Mg} (Mg/Mg + Mn + Fe_{tot}) in biotite, and Si content in white mica, and are shown on some pseudosections where they assist with further constraining P-T estimates. Fluid content was derived from the LOI value unless stated otherwise, and considered as pure H_2O in all calculations.

4.1 Kalak-Vaddas boundary – UL248

4.1.1 Petrography and mineral chemistry

Sample UL248 (Fig. 2, 3, 4B; Table 1) represents a mylonitized equivalent of migmatitic paragneisses from the upper part of the KNC (Fig. 4A). The fine-grained matrix of sample UL248 contains porphyroblasts of garnet (up to 0.9 mm) and fragments (up to 5 mm) of plagioclase, K-feldspar and quartz-feldspar aggregates (Fig. 4C). Biotite, muscovite and elongate grains and aggregates of quartz and feldspar define the S2 mylonitic foliation. Two generations of muscovite are found as 1) rare large (~200 mm) mica fish parallel to the S2 foliation (Ms1), and 2) as small grains intergrown with biotite and along garnet and K-feldspar boundaries, within the S2 foliation (Ms2). Quartz, biotite and rutile are common as inclusions in garnet (Fig. 4C). Minor rutile is also found in the matrix. Titanite is abundant as elongate 20-350 mm-long grains parallel to the S2 foliation and as inclusions in garnet rims (Fig. 4C, 6A). Distinctive garnet zoning displays two generations of garnet. Garnet cores (Grt1) have a relatively flat compositional profile, followed by a transition zone, to a ~100-150 mm-thick rim (Grt2; Fig. 6A). The two generations show significantly different compositions. Grt1 is lower in Grs (Grs_{10-12}), higher in spessartine (Sps_{12-15}), and has a higher X_{Mg} content (0.11-0.13) than Grt2. Grt2 displays the following composition: Grs_{36-38}, Sps_{3-4} and X_{Mg} content of 0.08-0.11. Grt2 (rims) grew together with biotite, titanite, plagioclase (rims) and Ms2 during top-to-SE S2 shearing. X_{Mg} in biotite ranges between 0.36 and 0.45. Plagioclase generally shows zoning with a higher anorthite content in the cores (An_{25-28}) than rims (An_{20-23}). Early muscovite (Ms1) has a Si content between 3.06 and 3.08 (a.p.f.u.). Later muscovite (Ms2), associated with S2 shearing, has a higher Si content, between 3.20-3.27

(a.p.f.u.; Table 4). The relict compositions shown by Grt1, plagioclase cores and large Ms1 fish indicate that earlier P-T conditions may have been preserved by the sample.

4.1.2 P-T Modelling

The difference in composition between garnet cores and rims suggests that the cores represent an early P-T history and were shielded from equilibration with the matrix by garnet rims. The conditions for garnet core and rim formation were therefore modelled separately. An estimate for conditions during garnet core formation was modelled using the composition obtained from the bulk rock XRF analysis (Table S1). Since leucosome was observed in less sheared outcrops of the same rock type within 10 m of the sample site, garnet cores in the sample were modelled as part of a migmatite assemblage. An approximate pressure was estimated to be 10 kbar from the position of garnet isopleths representing measured garnet core compositions in a water-saturated pseudosection. Water content for modelling this event was then estimated from the position of the solidus in a T-X_{H2O} pseudosection calculated at 10 kbar. In Figure 7A modelled X_{Mg}, Sps and Grs compositions fit measured garnet core compositions within the phase field Grt-Bt-Pl-Kfs-Ms-Rt-Qtz-Melt, constraining pre-S2 conditions to 705-735 °C and 9.9-10.8 kbar. As diffusion in garnet at upper amphibolite facies conditions during the overprinting event is considered to be fast (e.g. Caddick et al., 2010), care should be taken with interpreting these as absolute P-T conditions as garnet cores could have been modified by diffusion. However we consider that the shape of the garnet profile indicates that diffusion of Grt2 boundaries is shown by the transition zone between Grt1 cores and Grt2 rims, and that the flat cores probably represent Grt1 that escaped diffusion during S2 overprinting (Fig. 6A). The estimate is consistent with the presence of rutile, and a lack of titanite as inclusions in garnet cores (Fig. 4C, 6A). It also agrees well with the anorthite (An_{25-29}) content in zoned plagioclase cores and Si content of large Ms1 mica fish (Table 4).

The P-T estimate for garnet rim and S2 formation (Fig. 7B) was calculated with the XRF bulk rock composition from which garnet cores were subtracted by using the modal Grt1 proportion estimated from the pseudosection (0.75 modal%). LOI from the bulk rock

analysis was used as H_2O content. Modelled X_{Mg}, Sps and Grs compositions fit measured garnet rim compositions in the phase field Grt-Bt-Ms-Pl-Kfs-Ttn-Rt-Qtz, and constrain S2 shearing to 635-690 °C and 11.5 – 12.3 kbar (Fig. 7B). Anorthite content in plagioclase rims, X_{Mg} content in matrix biotite, and Si content of Ms2 agree well with this estimate. Titanite is predicted as part of the assemblage and is absent in the assemblage associated with garnet core formation, which is consistent with the large amount of titanite in the matrix and as inclusions in Grt2 (Fig. 4C, 6A). Based on field structural observations we interpret this P-T estimate for S2 to represent shearing along KNC-Vaddas boundary, and titanite growth is directly related to this event.

4.2 Upper Vaddas Nappe (AR71)

4.2.1 Petrography and mineral chemistry

Sample AR71 (Fig 2, 3; Table 1) is a medium-grained garnet-mica-schist with a strong S2 foliation defined by intergrown biotite and muscovite (Fig. 4F). Muscovite is the dominant mica and occurs as large (1-3 mm long) mica fish. Plagioclase is found as rare porphyroclasts and as singular recrystallized grains within quartz layers. Rutile is abundant as elongate grains parallel to the foliation (Fig. 4F). Minor ilmenite occurs as rims on rutile grains. Garnet grains are found as small (0.03-0.1 mm), singular, idiomorphic grains and as larger (1-2 mm) fish-shaped clusters of grains parallel to the foliation, with a synkinematic geometry displaying typical Caledonian top-to-SE shear sense (Fig. 4F). Garnet shows an almost flat compositional profile with slight variation between cores, mid-garnet and rims. In rare cases fish-shaped garnets have a thin rim of a different composition. These rims only occur at the apex of fish-shaped garnets and are never present on the S2 parallel rims, indicating that they represent growth of garnet during late S2 shearing (e.g. Fig. 6B, Table 3). In garnets that do not display the thin rim X_{Mg} varies from 0.17 in the cores to 0.14 in the mid-garnet and rims. Grs is slightly lower in cores (Grs_{7-8}) than mid-garnet and rims (Grs_{9-10}). Sps content varies between $Sps_{1.4-1.6.}$ Almandine content varies between Alm_{68-73} (Fig. 6B, Table 3). The thin garnet rims display the following composition: Alm_{65-67} Grs_{14-16} $Sps_{1.2}$ and an X_{Mg} of ~0.11 (e.g. Fig. 6B, Table 3). X_{Mg} in biotite ranges between 0.50 and 0.53, Si content in muscovite is

between 3.05 and 3.11 (a.p.f.u.), and plagioclase has an anorthite content of $An_{18–20}$ (Table 4).

4.2.2 P-T Modelling

Modelled X_{Mg}, Grs and Sps isopleths for cores, mid-garnet and normal rims corresponding to the observed composition of garnet and biotite intersect in the Grt-Bt-Pl-Ms-Pg-Qtz-Rt-H_2O phase field (Fig. 7C). This is consistent with the assemblage observed in the sample with the exception of paragonite, which was not observed but is predicted to be present only in small amounts (< 2 modal%). The slightly lower Grs, and higher X_{Mg} contents of the cores indicate that minor garnet zoning resulted from growth during an increase in pressure (Fig. 7C). Si content in muscovite was used to better constrain pressure range due to the pressure insensitive orientation of garnet isopleths in the phase field. Together with garnet compositions, the Si content of muscovite constrains an estimate of 630-640 °C and 11.7-13 kbar for S2 metamorphism and shearing (Fig. 7C), with cores forming between 11.7 and 12.2 kbar and mid-garnet and normal rims forming up to ~13 kbar. The model anorthite content in plagioclase at the estimated P-T conditions indicates that plagioclase is more albitic than expected for the estimated conditions. This suggests that plagioclase may have equilibrated towards lower P-T during shearing. The higher Grs and lower X_{Mg} contents, and a similar Sps content in the rare thin rims on garnet indicate retrogression to lower temperature, and probably lower pressure conditions along with growth of ilmenite rims on rutile (Fig. 7C; white arrow). The lack of an older foliation in the sample or in the outcrop, and the zoning pattern of garnet leads us to interpret that the Vaddas nappe was only affected by S2 Caledonian metamorphism and subsequently retrogressed to lower P-T conditions.

4.3 Kåfjord Nappe (AR153)

4.3.1 Petrography and mineral chemistry

Sample AR153 (Fig. 2, 3; Table 1) is a medium- to fine-grained garnet-biotite-zoisite schist. It is taken from the lower Kåfjord and considered to represent metamorphosed sediments. Biotite, minor muscovite, zoisite and elongate quartz-feldspar aggregates define a strong mylonitic S2 foliation (Fig. 4I). Garnet is porphyroblastic and

idiomorphic and often has inclusion-rich cores and inclusion-poor rims. Cores include quartz, biotite, ilmenite and chlorite (Fig. 4H). Chlorite is absent in the matrix. Rutile and titanite are both found as elongate grains parallel to the foliation, although rutile is significantly more abundant. Two generations of ilmenite occur as small inclusions in garnet and as thin rims on rutile grains (Fig. 4H, 4I). Garnet shows some compositional change from core to rim (Fig. 6C; Table 3). Alm content is variable across the garnet (between Alm_{53-62}). Grs content is around 20-21% in the cores and increases towards rims up to between 22 and 27%. X_{Mg} in the profile (Fig. 6C) does not vary significantly between cores and rims (between 0.15-0.18, although spot analyses show that X_{Mg} is often lower in cores than in the rims (Table 3). Sps content is higher in the cores (4-5 mol%) than in the garnet rims (1-2 mol%). Plagioclase shows no zoning, and has a composition between An_{25}-An_{31}. X_{Mg} in biotite is between 0.56 and 0.60. Si content of the white mica is between 3.16 and 3.2 (a.p.f.u.).

4.3.2 P-T Modelling

Zoning in garnet and the difference between garnet inclusion assemblage and matrix assemblage suggest the rock records evolving P-T conditions. The presence of chlorite and ilmenite as inclusions in garnet (Fig. 4H. I) indicate that the cores grew at different conditions relative to rims and the matrix. Garnet cores show a relatively higher Sps content and lower content of Grs than rims. Modelled X_{Mg}, Grs and Sps isopleths are consistent with measured garnet core composition within the phase fields Grt-Bt-Pl-Ilm-Qtz ± Chl ±H_2O, and constrains garnet core growth to 590 – 625 °C and 5.9-6.9 kbar (Fig. 7D). Modelled X_{Mg}, Grs and Sps isopleths representing measured garnet rim compositions plot within the phase field Grt-Bt-Pl-Ms-Zo-Rt-Qtz-H_2O, which is consistent with the matrix assemblage (Fig. 4I). The morphology of the isopleths is consistent with a lack of significant zoning in pyrope (and X_{Mg} content) in the garnets. A match of model compositions for the rim estimate is also observed with the measured plagioclase composition, and Si content in muscovite. Sps, X_{Mg} and Grs isopleths and anorthite content in plagioclase were used to constrain the peak metamorphism at 600 – 660 °C and 9.8 – 11 kbar (Fig. 7D). X_{Mg} value of biotite in the sample has a large range that is consistent with modelled values for both the garnet core and rim estimates, and

which is likely the result of biotite growth and equilibration over evolving P-T conditions. There is no microstructural evidence to suggest that there is more than one generation of biotite. The shape of the garnet compositional profile (Fig. 6C) compared against the morphology of the isopleths on the pseudosection suggests continuous garnet growth with increasing pressure (and slightly increasing temperature). Ilmenite rims on rutile grains are likely a result of later retrogression.

4.4 Nordmannvik Nappe – migmatite (AR25b)

4.4.1 Petrography and mineral chemistry

Sample AR25b (Figs. 2, 3; Table 1) is a coarse-grained migmatitic paragneiss with leucosome segregations and dark restitic layers (Figs. 5E, F). It has a macroscopic weak foliation defined by biotite and migmatitic banding. The leucosome consists of plagioclase, quartz and K-feldspar (partly replaced by myrmekite). Kyanite and garnet porphyroblasts (2-3 mm in size) are common along leucosome boundaries and in the restite (Figs. 5F). Kyanite occurs as large (up to 6 mm) porphyroblasts oriented both randomly and parallel to the foliation. It is almost always in association with biotite, and often with quartz (Fig. 5F). Kyanite crystals sometimes contain inclusions of quartz and biotite, and are occasionally in grain contact with garnet. Smaller kyanite crystals are also found as inclusions in quartz in leucosomes. Garnets do not have a large number of inclusions, although sillimanite inclusions do occur (confirmed by Raman spectra; Fig. 8), and in minor amounts, fine-grained sillimanite is intergrown with biotite or occurs along some kyanite and garnet rims. Muscovite occurs as rare small grains overgrowing biotite and is often associated with fine-grained sillimanite. Garnet is usually idiomorphic, and contains inclusions of sillimanite, biotite, quartz and ilmenite (Fig. 8, 9A). Garnets show a profile with a relatively flat core and gradual zoning near the rims, probably indicative of diffusion zoning. Garnet core and rim compositions are similar. X_{Mg} in garnet cores is between 0.23-0.26 and decreases in the rims to 0.20-0.23. Alm in cores is between 65-69 mol% and rims between 69 and 71 mol%. Grs in garnet cores is as low as 4.5 mol% and at the rims is between 6 -7 mol%. Sps content of garnet cores is 3 mol% and at rims is between 3.5 - 4 mol% (Fig. 9A).

4.4.2 P-T Modelling

Metamorphic conditions for the migmatitic S1 foliation in the Nordmannvik Nappe were estimated from sample AR25b (Fig. 10A). To estimate water content for migmatisation first an approximate pressure for equilibration was estimated from a water-saturated pseudosection using the XRF bulk composition. Isopleths for Grs, Sps and X_{Mg} contents intersect at ~10 kbar. Water content was then estimated from the position of the solidus on a T-X_{H2O} pseudosection calculated at 10 kbar for the mineral assemblage associated with melting. The presence of kyanite and sillimanite, together with the variation in plagioclase and biotite composition suggest that the minerals record evolving metamorphic conditions. The flat profile for garnet cores and zoning at the rims suggests garnets had a homogenous composition and rims may have been modified by diffusion during conditions out of equilibrium with garnet cores (Fig. 9A). The association of kyanite, biotite and garnet with the leucosome in the S1 foliation suggests these minerals formed the stable assemblage during S1 partial melting. Given the large volume of kyanite associated with the leucosome, kyanite is related to the majority of the partial melting probably by the following reaction: Ms ± Pl + Qtz = Kfs + Als + Liq. This is consistent with the lack of muscovite in the rock and presence of K-feldpar. Based on the relationship between garnet rims and the leucosome, garnet rim compositions were taken as representative of S1 migmatization conditions.

The majority of measured garnet rim compositions and some mid-garnet compositions correspond with modelled isopleths in the phase field Grt-Bt-Pl-Kfs-Ky-Qtz-Melt on the pseudosection (Fig. 10A). X_{Mg}, Grs and Sps contents from these analyses constrain S1 partial melting to 760 – 790 °C and 9.4 – 11 kbar. Several measured garnet rims also correspond with modelled isopleths below the solidus within the muscovite-bearing assemblage, consistent with cooling, and late muscovite growth in the sample and late minor diffusional resetting of garnet rims. The minor fine-grained sillimanite with biotite and along kyanite and garnet rims is consistent with retrogression to lower pressures.

The homogenous garnet core compositions were also plotted on the pseudosection (Fig. 10A) and modelled isopleths for Grs, Sps and X_{Mg} contents correspond with measured

contents in the sillimanite-bearing phase field (Grt-Bt-Pl-Kfs-Sill-Qtz-Melt) above the solidus at 790 – 815 °C and 8.9 – 9.9 kbar (Fig. 10A). These conditions show similar temperatures to the S1 melting conditions, but slightly lower pressures. The range in measured X_{Mg} content of biotite corresponds with isopleths that plot consistently with both estimates, whereas measured anorthite content for matrix plagioclase corresponds with isopleths that plot toward the lower pressure conditions (sillimanite-bearing assemblage). It should be noted that the estimated conditions for garnet core formation are apparent conditions as cores were probably re-equilibrated by diffusion during the later kyanite-melting event. However, the presence of sillimanite inclusions in garnet (Fig. 8) is consistent with the estimated conditions.

The relationship between garnet core and rim conditions and what they might represent is difficult to interpret. Since the garnets do not show two generations, and have probably been re-equilibrated during diffusion, garnet core and rim compositions likely represent metamorphism during one event. If this is the case, the estimates that have been constrained from core and rim compositions suggest that migmatization began at low pressures and continued at higher pressures. A scenario such as this is difficult to reconcile because the melting reaction is almost completely temperature-dependent, and therefore the bulk of melting would have occurred at the lower pressure sillimanite-present conditions and no or little melt produced with a pressure increase. This is contrast to the microstructures that suggest partial melting produced mainly kyanite. We therefore conclude that garnet core compositions probably do not record a real earlier partial melting event as this would make subsequent melting at higher-pressure conditions challenging.

4.5 Nordmannvik Nappe – mylonite (AR26)

4.5.1 Petrography and mineral chemistry

Sample AR26 (Fig. 2, 3; Table 1) is a fine-grained schist that displays a pervasive mylonitic S2 foliation defined by biotite, muscovite, and kyanite (Fig. 5B). It has a strong L2 stretching lineation defined by quartz aggregates. Plagioclase sometimes forms 0.1-0.3 mm-sized sigma clasts. Biotite occurs as two generations; less common large

foliation-parallel grains, and as finer grained elongate grains intergrown with muscovite (e.g. Fig. 5B). Muscovite occurs as mica fish parallel to the foliation, and as rare late grains that crosscut the foliation (Fig. 5B). Garnet is found as large 1-2 mm idiomorphic porphyroblasts (Fig. 9B) that sometimes have inclusion-poor cores (with occasional sillimanite) and more inclusion rich rims (quartz and biotite inclusions), and as small 0.1-0.4 mm idiomorphic grains that occur singularly (Fig. 9C) or as clusters oriented parallel to the S2 foliation. The bimodal garnet grain size is also observed in hand specimen and therefore not an apparent difference caused by sectioning effect.

The larger garnets display a slight difference in composition relative to the smaller garnets. Their X_{Mg} contents are similar, however the larger garnets have a slightly lower Sps content ($Sps_{1\text{-}1.5}$) than the smaller garnets ($Sps_{2.5\text{-}3.5}$) and a lower Grs content ($Grs_{4\text{-}5}$) than smaller garnets ($Grs_{5\text{-}6}$). Almandine content in the larger garnets ($Alm_{71\text{-}76}$) is higher than in the smaller garnets ($Alm_{65\text{-}72}$; Fig. 9B, C, Table 3).
Thin rims on larger garnets sometimes show similar compositions to the small garnets. The garnet profiles for the large and small garnets are similar, although larger garnets have a wider flat profile for their cores. Grs is the only garnet end-member that reflects the apparent zoning displayed by garnet microstructure in the larger garnets (Fig. 9B). It displays a slightly lower content for the nearly inclusion-free cores (Fig. 9B, grey box) and a slightly higher, flat profile in the inclusion-rich rims. The larger garnets also have a thin 10-20 μm-wide rim (Fig. 9B; dark grey box) with lower X_{Mg} values and Grs contents than cores. Smaller garnets have a similar profile but lack the wide flat cores, and have compositions similar to those of the rims of larger garnets (Fig. 9C). Based on the similarity in garnet rim compositions, and that most garnet end-members do not show zoning reflecting the garnet microstructure, the zoning in both the large and small garnets probably resulted from diffusion during high-grade metamorphism. The smaller garnets are probably more completely re-equilibrated than the larger ones. The two generations of biotite have different compositions. Older biotite has an X_{Mg} between 0.56-0.58, closer to the composition of inclusions in garnet (X_{Mg} ~0.6). Younger biotite displays X_{Mg} values between 0.46-0.48. Plagioclase is unzoned with a composition of $An_{23\text{-}24}$ (Table 4).

4.5.2 P-T Modelling

The variations in mineral compositions of the sample likely reflect changing P-T conditions with time. The profile shape and compositions of the larger and smaller garnets suggest that both probably started with the same homogenous composition and smaller garnets re-equilibrated more completely than large ones during diffusion associated metamorphism and S2 shearing (e.g. Caddick et al., 2010). Therefore the cores of larger garnets may reflect earlier P-T conditions. Biotite, kyanite and muscovite are in contact with garnet rims and define a clear S2 foliation associated with subsolidus shearing. X_{Mg}, Sps and Grs compositions of the smaller re-equilibrated garnets and some larger garnet rims agree with modelled isopleths in the Grt-Bt-Pl-Kfs-Ms-Ky-Qtz phase field, and constrain S2 shearing to 680 – 730 °C and 9.5 – 10.9 kbar (Fig. 10B). Measured X_{Mg} values for the younger biotite generation and Si content in muscovite agree well with their respective modelled isopleths for this estimate. The Grs, Sps and X_{Mg} contents of larger garnet cores (e.g. Fig. 9B, light grey box) are consistent with modelled isopleths that plot within the Grt-Bt-Pl-Kfs-Ky-Qtz-Melt and Grt-Bt-Pl-Kfs-Sil-Qtz-Melt phase fields at 790 – 810 °C and 8 – 10.4 kbar (Fig. 10B). Since the rock has been overprinted strongly by the S2 foliation this early estimate reflects an apparent P-T for a possible earlier event (S1 melting or earlier?), although garnet compositions have been affected by later diffusion. However it should be noted that the apparent garnet core estimate agrees with the presence of sillimanite inclusions in garnet cores, the measured X_{Mg} content of biotite inclusions in garnet, and anorthite content of plagioclase sigma clasts in the matrix, suggesting that garnet is not the only mineral that records this earlier P-T evolution.

5 Geochronology

In order to temporally constrain the metamorphic and deformation history of the RNC, zircon and titanite from several tectonic levels were selected for geochronology.

5.1 S1 Melting in the Nordmannvik Nappe – U-Pb SIMS dating of zircon

Sample AR23a (Fig. 2, 3; Table 1) was cut in an attempt to obtain different zircon populations for the restite and leucosome layers in Nordmannvik migmatite. Zircon from

the restite is represented by clear, euhedral, and prismatic crystals between 100 and 350 μm-long. All grains have low CL-emission (dark grains) and show weak oscillatory zoning (Fig. 11A). Five grains have brighter rounded cores with discrete boundaries, indicative of a possible xenocrystic origin. Zircon from the leucosome is slightly larger than the grains from the restite. The grains are clear or yellow-orange in colour, and form euhedral prismatic crystals 150-350 μm-long. Under CL they are equally dark and show similar weak oscillatory zoning to the zircon from the restite, however inherited cores are absent (Fig. 11D). For the restite, 37 spots were analyzed in 26 grains. Five of the analyses are from the bright cores. These cores have U/Th ratios between 0.3-0.53. Two of the core analyses plot on concordia, two plot close, and one is strongly discordant (Fig. 11B, grey ellipses). The discordant analysis is likely due to mixing of a CL-bright core and darker rim. Of the four analyses that plot on or near concordia, the oldest three give $^{207}Pb/^{206}Pb$ dates of 1836 ± 10 Ma, 1721 ± 10 Ma, and 1599 ± 14 Ma. The fourth core gives a younger $^{206}Pb/^{238}U$ date of 585 ± 8 Ma. The remaining 32 analyses are from regions in zircon grains that show low CL-emission and weak oscillatory zoning. They have U/Th ratios between 0.09 and 0.16, overlap on concordia and give a combined concordia age of 442 ± 2 Ma (Fig. 11C). For the leucosome, 27 spots were analyzed in 18 grains from both light and dark CL-zones in the zircon crystals. They have U/Th ratios of 0.08 to 0.19, and form a cluster on concordia giving a concordia age of 439 ± 2 Ma (Fig. 11E). The concordia age for the leucosome is slightly younger than, although within error of, the restite concordia age. The oscillatory zoning patterns in the zircons from both the restite and leucosome populations and the shape of the zircons suggest they have crystallized from melt (e.g. Hoskin and Schaltegger, 2003).

5.2 Metamorphism in the Nordmannvik Nappe – U-Pb dating of titanite

Sample A01 is a coarse-grained felsic rock formed in the interaction zone between melt and calc-silicate rocks in the Nordmannvik Nappe on Arnøya (Figs. 2, 3, 11F, G; Table 1). The sample is comprised of K-feldspar, quartz and plagioclase and randomly oriented mafic schlieren including mainly clinopyroxene with amphibole, plagioclase, biotite, quartz, titanite, and minor calcite, ilmenite, magnetite, and iron sulphides. No foliation is present in the sample. Titanite is abundant and coarse-grained (up to 2 mm in size: Fig.

11G). It occurs as large euhedral grains mainly in the boundary zone between the schlieren and the felsic zones and is either associated with magnetite and quartz, or as inclusions in the rims of amphibole grains. It also sometimes occurs as thick rims on ilmenite. Six clear-brown 300 – 600 μm sub- to euhedral titanite fragments were analyzed using the TIMS method. All analyses plot on concordia and 4 of them overlap (in bold; Fig. 11H) giving a combined concordia age of 432 ± 1 Ma. An older grain with a $^{206}Pb/^{238}U$ age of 440 ± 4 Ma and a younger grain with a $^{206}Pb/^{238}U$ age 428 ± 1 Ma do not overlap with these analyses and these were not involved in the calculation of the concordia age. Together these ages indicate a range between 444 and 427 Ma, with a peak at ~432 Ma. These ages are interpreted to represent metamorphism in the Nordmannvik nappe.

5.3 Gabbro intrusion in the Vaddas Nappe – U-Pb SIMS dating of zircon

Sample SK18b was taken from a late-stage pegmatitic gabbro-lens within the main, medium-grained Kågen gabbro in the Vaddas Nappe (Figs. 2, 12A). It is coarse-grained and consists predominantly of up to 1 cm-long amphibole crystals in a plagioclase matrix. Zircons from the sample are euhedral, short-prismatic, and between 100-300 μm long. Under CL grains are variable. The dominant type has a darker core and goes over into a CL bright rim. Less common types of zircon display a bright core and dark rim, or are almost completely CL dark (Fig. 12B). Twenty spots were analysed in 16 grains. Th/U values are between 0.3 and 0.7, consistent with zircon crystallization from a melt. All analyses are concordant giving a concordia age of 439 ± 1 Ma (Fig. 12C), interpreted as the intrusive age for late-stage gabbroic pegmatites within the Kågen gabbro.

5.4 S2 shearing at the Vaddas-Kalak boundary – U-Pb titanite ages

Microstructural observations and P-T modeling show that titanite crystallization in sample UL248 is associated with S2 shearing and metamorphism during garnet rim growth (Fig. 4C, 6A). Titanite from the sample was therefore dated using TIMS. The majority of picked titanite grains have inclusions and the three cleanest fragments were chosen for TIMS analysis. They are pale brown 240-300 μm-long, inclusion-free grains. All three analyses plot on Concordia with $^{238}U/^{206}Pb$ dates between 436 ± 4 Ma and 431 ±

2 Ma (Fig. 11D). The mean $^{238}U/^{206}Pb$ age is calculated as 432 ± 6 Ma. We interpret this age to represent the age of S2 shearing and metamorphism along the KNC-Vaddas boundary, and the likely emplacement age of the Vaddas Nappe over the KNC.

6. Metamorphic and magmatic evolution of the RNC

6.1 Potential early metamorphic events

A potential early metamorphic event is preserved in one sample. Garnet zoning in sample UL248 is clear (KNC-Vaddas boundary). Grt1 formed at 705-735 °C and 9.9-10.8 kbar above the solidus (Fig. 7A) at higher temperature and lower pressure than Grt2 (Fig. 7B, 13A). Sheared and dismembered leucosome suggests that melt solidified and was subsequently sheared during S2 overprinting. The sample site is situated below the KNC-Vaddas boundary within the KNC. Caledonian-age migmatization has not been recorded in the KNC in the area, and the conditions for Grt1 are similar to those recorded for partial melting in the KNC at Eide nearby, at 702 ± 5 Ma (~730–775 °C and ~6.3–9.8 kbar; Gasser et al., 2015; Fig. 13A, B). We therefore suggest that Grt1 in sample UL248 records the same pre-Caledonian partial melting recognized at Eide. Further work needs to be done to establish this age better. Evidence for events and foliations this age in the RNC is lacking.

Garnets in the lower Kåfjord Nappe sample (AR153) show a different history, with core growth recording lower amphibolite facies conditions (590-625 °C and 5.9 – 6.9 kbar; Figs. 7D, 13A). The P-T estimate is consistent with a slightly elevated geothermal gradient of 27 – 30 °C/km. Without direct age dating it is difficult to give the exact timing of this event. However, the continuous growth zoning in the garnet probably records increasing pressure during S2 shearing (Fig. 6C, 8D) and the lack of pre-S2 foliation in the Kåfjord Nappe suggest that the garnets record early growth during Caledonian S2 shearing (Fig. 13A, B). The pressure conditions estimated for this event are within range of the pressure conditions estimated for gabbro intrusion in the Vaddas Nappe, indicating that the two events may be related (7-9 kbar; Getsinger et al., 2015).

6.2 Migmatisation in the Nordmannvik Nappe

In the Nordmannvik nappe early high-grade metamorphism is preserved by an S1 migmatitic foliation in lower strain lenses. Phase equilibrium modelling of this foliation reveals that garnet cores in the Nordmannvik Nappe samples, AR25b and AR26, show apparent high temperature- mid- to low- pressure partial melting in the sillimanite and kyanite stability fields. In sample AR25b the garnet cores and rims separate partial melting into two relative sets of conditions at low-pressure, high-temperature (790 – 815 °C and 8.9 – 9.9 kbar) and higher pressure lower-temperature (760 – 790 °C and 9.4 – 11 kbar: Figs. 10A, 13A). In sample AR26 conditions similar to the range of both estimates in sample AR25b are constrained from garnet core compositions to 790 – 810 °C and 8 – 10.4 kbar in the kyanite and sillimanite fields (Figs. 10B, 13A). Despite the presence of sillimanite inclusions in garnet cores, it is unclear how real the lower-pressure partial melting estimates for garnet cores in these samples are, as the majority of partial melting occurred in the kyanite stability field and cannot have resulted from a pressure increase during a shift from the sillimanite-stability field towards the kyanite stability field. It is, however, likely that garnet cores record conditions that are not real as they have been affected by diffusion during kyanite-grade S1 partial melting and S2 shearing (e.g. Caddick et al., 2010).

We therefore suggest that either: 1) S1 migmatization occurred around the kyanite-sillimanite reaction curve and a transient geotherm led to the majority of melting within the kyanite-stability field with preservation of sillimanite in some garnet cores, or 2) that the garnet core conditions are only apparent and diffusion has led to re-equilibration of garnet so that earlier conditions are no longer preserved. In this case sillimanite inclusions could have formed at any time, e.g. during solid-state prograde metamorphism associated with the S1 partial melting event, or during an unknown pre-Caledonian metamorphic event, the conditions of which we cannot constrain. Polymetamorphism in the Nordmannvik nappe has been previously related to Precambrian or Ordovician events (Elvevold et al., 1987; Lindstrøm and Andresen, 1992), however we see no structural or geochronological evidence to suggest pre-Caledonian metamorphism or deformation affected the Nordmannvik Nappe.

Leucosome associated with partial melting and formation of the kyanite-bearing S1 foliation crystallized between ~443-437 Ma (Fig. 11A-E, Fig. 13B). This indicates early Silurian melting in the lower crust with a geothermal gradient between 22-25 °C/km. The presence of partial melt preserved in the axial planes of Caledonian folds in the Nordmannvik Nappe (Fig. 5D) indicates that the rocks were partially molten during Caledonian shearing. The rocks are also overprinted by the solid-state Caledonian S2 shear foliation (Figs. 5A, C). Considered together, these structures indicate that the Nordmannvik Nappe migmatites underwent initial Caledonian shearing while still partially molten, and continued shearing as they solidified with final S2 overprinting in their solid-state. This progression can be seen by the anticlockwise P-T path formed between S1 and S2 conditions (Fig. 13A).

Peak metamorphic conditions for sample A01 are expected to be similar to those recorded by the nearby migmatitic metapelites in the Nordmannvik Nappe (Fig. 10A) as it was sampled from a similar low strain lens to sample AR25b. Little macroscopic S2 overprinting is present (Fig. 11F). Its microstructural relationships indicate titanite formed from interaction between melt and the calc-silicate rocks. Therefore the range in titanite ages for the sample (444-427 Ma) is unexpected. This range could be the result of either 1) diffusional Pb loss during cooling above the closure temperature of titanite (e.g. Tucker et al., 2004), or 2) protracted titanite growth during cooling (Kohn, 2017). The closure temperature of titanite is debated (e.g. Cherniak, 1993; Frost et al., 2001), although recent well-constrained work in the Western Gneiss Region suggests Pb diffusion in titanite is slow (Spencer et al., 2013; Kohn et al., 2015) and probably ineffective below 800 °C (Kohn 2017). The large grain size (> 300 μm) of the titanites in sample A01, and estimates for both S1 and S2 P-T conditions < 800 °C suggest it is unlikely that diffusional Pb loss caused the large age range, and from this we conclude that titanite probably grew over a protracted time period and records some long-lived metamorphic process.

The association between titanite grains, magnetite and quartz, and titanite and amphibole suggest that it formed by rehydration (1: Cpx + Ilm + Qtz + H_2O = Amph + Ttn) and/or oxidation (2: Cpx + Ilm + O_2 = Ttn + Mag + Qtz) reactions (e.g. Kohn, 2017) during crystallization of melt within calc-silicate layers. Both reactions are consistent with the observation of titanite rims on ilmenite grains. If both reactions were active, then prolonged titanite growth from ~444-427 Ma in the Nordmannvik rocks is probably resulted from switching between one reaction to the other during evolution of the system, controlled by H_2O and O_2 availability from injected melt and metamorphic fluids. And although the rocks do not record the Caledonian S2 shear foliation, they record long-lived titanite growth probably driven by melt and/or fluid infiltration during prolongued Caledonian metamorphism. Both the zircon and titanite ages are consistent with the 439 ± 1 Ma metamorphic age (from zircon overgrowths) reported from the Nordmannvik Nappe at Heia (Augland et al., 2014).

6.3 Gabbro intrusion in the Vaddas nappe

Coeval with S1 migmatitization in the Nordmannvik Nappe, late-stage gabbroic pegmatites intruded the Vaddas Nappe on Kågen at 439 ± 1 Ma (Figs. 12A, B, 13B) at depths of 7 – 9 kbar (Getsinger et al., 2013). These data suggest that the Kågen gabbro intruded the Vaddas metasediments at a depth of 20-30 km, with the final stages of magmatism occurring at 439 ± 1 Ma. The gabbroic composition clearly indicates a mantle source of the melt, and the tholeiitic composition, measured from other mafic rocks and gabbros in the nappe (Lindahl et al., 2005), suggests the gabbro intrusions in the Vaddas nappe probably occurred in an extensional setting. The small gabbro bodies in the Kåfjord Nappe are probably also related to this event. The intrusion of the Kågen gabbro at 439 ± 1 Ma is slightly earlier than intrusion of the Heia gabbro in the Nordmannvik Nappe (435 ± 1 Ma ; Augland et al., 2014). Similar mafic intrusive rocks, also of early Silurian age, in the Narvik Nappe Complex (Råå intrusion; 437 ± 0.5 Ma; Tucker et al., 1990), the Vaddas/Kalak Nappe (Halti Igneous Complex; 434 ± 5 Ma and 438 ± 5 Ma; Vaasjoki and Sipilä, 2001; Andréasson et al., 2003), and granitic and gabbroic rocks on Magerøy (intruded between 440-435 Ma; Kirkland et al., 2005; Corfu et al., 2011) suggest that this magmatic intrusive event was relatively short-lived but

widespread in northern Norway within rocks at roughly the same mid- to lower crustal tectonostratigraphic level.

6.4 Pervasive S2 shearing

Pervasive, amphibolite-facies S2 shearing with top-to-SE kinematics is recorded throughout the entire RNC. Conditions of S2 shearing in the all three nappes record temperatures between ~600 – 700 °C and pressures between 9.5 – 13 kbar (Fig. 13A), indicating nappe stacking related to the S2 foliation occurred at mid- to lower-crustal conditions (~32-43 km depth). These conditions of S2 metamorphism also indicate a relatively cool geotherm (16-19 °C/km). The KNC-Vaddas boundary rocks record S2 shearing at 635-690 °C and 11.5 - 12.3 kbar at similar conditions (within error) to the conditions of metamorphism in the Vaddas Nappe (630-640 °C and 11.7-13 kbar; Figs. 7C, 13A), indicating metamorphism around ~37-43 km depth during shearing between the lower RNC and the underlying KNC. Garnets in the Kåfjord Nappe records not only peak S2 pressure conditions (garnet rims: 600 – 660 °C and 9.8 – 11.2 kbar), but also the P-T path showing an increase in pressure from lower P-T conditions, associating S2 shearing with crustal thickening during continental collision (Figs. 7D, 13A). S2 shearing in the Nordmannvik Nappe is recorded in the mylonitic gneisses near the Kåfjord-Nordmannvik boundary at 680 – 730 °C and 9.5 – 10.9 kbar (Figs. 10B, 13A). Considering a maximum error on the P-T conditions of ± 50 °C and 1 kbar, the estimates for S2 in the three nappes are similar. Although a relative trend shows an increase in pressure for S2 conditions downwards in the RNC and an increase in temperature upwards, indicating an inverted temperature gradient (Fig. 13A).

The age of S2 shearing along the KNC-Vaddas boundary is constrained by syn-S2 titanite at 432 ± 6 Ma (Figs. 12D, 13B), and probably records stacking of the Vaddas nappe over the KNC. The younger titanite ages in the Nordmannvik nappe rocks (433-428 Ma; Fig. 13B) probably also record S2 shearing related to metamorphic fluid infiltration in the calc-silicate rocks. The age of S2 metamorphism is consistent with ages for Caledonian metamorphism in the equivalent Magerøy Nappe (Corfu et al., 2006, 2011; Kirkland et

al., 2005, 2016), Narvik Nappe Complex (Augland et al., 2014) and upper KNC (Kirkland et al., 2007a; Gasser et al., 2015).

6.5 An anticlockwise P-T path for Caledonian metamorphism in the RNC

Both the Nordmannvik rocks and the Vaddas/Kåfjord metasediments display anticlockwise P-T paths. Anticlockwise P-T paths are typically observed where an initial heating event is followed by burial or cooling (Wakabayashi, 2004). Nappe stacking itself is not considered to be capable of providing the amount of heat required to explain the P-T signatures (e.g. Johnson and Strachan, 2006). In the Nordmannvik Nappe it is clear that initial higher temperature conditions preceded colder conditions associated with crustal thickening, and that deformation associated with crustal thickening began when the rocks were still partially molten (partial melting prior to ~440 Ma) and continued as they crystallized and deformed in the solid-state between 440-430 Ma. The Vaddas and lower Kåfjord metasediments considered together, also show an anticlockwise P-T path, at colder temperatures. The Kåfjord Nappe records an initial event at (< 23 km depth) with an elevated geotherm, followed by an increase in pressure associated with burial to ~35 km during crustal thickening (Fig. 13A). The similar Vaddas metasediments record peak pressure conditions during S2 shearing similar to the Kåfjord metasediments, and retrogression to lower P and T during exhumation (< 550 °C and < 10 kbar; Figs. 7C, 13A). The intrusion age of the gabbro into the Vaddas Nappe (439 ± 1 Ma) gives a contemporaneous age with metamorphism and S1 partial melting in the Nordmannvik Nappe (439 ± 2 Ma). Given that similar gabbros are observed throughout the Vaddas, Kåfjord and Nordmannvik nappes and the lack of earlier structures in the rocks it is likely that the garnet cores in the Kåfjord sample also record this heating event, but at a shallower level in the crust than the Nordmannvik Nappe. Considering the P-T conditions and ages together, Caledonian metamorphism in the RNC occurred along an anticlockwise P-T path, with an early heating and intrusion event affecting the rocks almost immediately prior to or during continental collision.

7 The tectonic evolution of the RNC

7.1 A note on protolith ages

In order to understand the relationships between the different nappes of the RNC and to reconstruct their tectonic evolution, the protolith ages of the metasedimentary rocks within the different nappes have to be known. The Vaddas and Kåfjord samples are metasedimentary rocks that seem to show no evidence for a pre-Caledonian metamorphic or deformation history, consistent with their proposed origin as late Ordovician/early Silurian sediments (e.g. Binns and Gayer, 1980). The Magerøy Nappe, considered equivalent to the Vaddas Nappe, gives a volcaniclastic age of 438 ± 4 Ma, indicating deposition during the early Silurian synchronous with intrusions into the rocks, and implying rapid burial of sediments (Kirkland et al., 2005, 2016). The age and pressure of the Kågen gabbro intrusion (439 ± 1 Ma and 7 - 9 kb; Getsinger et al., 2013) indicate that at this time these rocks were not in an oceanic tectonic realm but part of thickened crust. The protolith age of the Nordmannvik samples, however, is still unresolved. The presence of marble and calc-silicate suggests they were deposited as shallow water sediments, probably on a continental shelf. The large age range from inherited cores in zircon (1800 – 1600 Ma) may represent detrital ages from the original source rock, and are typical northern Norwegian Baltica intrusive ages (e.g Larson and Berglund, 1992). If interpreted as a detrital age, the youngest inherited core age of 585 ± 8 Ma would represent a late Neoproterozoic maximum depositional age for these rocks (Figs. 11A, 13B). Farther to the southwest, the Narvik Nappe Complex contains amphibolite-facies marbles at the same tectonostratigraphic level with a chemostratigraphic depositional age of 610-590 Ma (Augland et al., 2014; Melezhik et al., 2014), indicating that the Nordmannvik rocks could indeed represent Late Neoproterozoic deposits. Alternatively, if the sillimanite in garnet cores records some pre-Caledonian metamorphic event, then the youngest inherited core age might not represent a detrital age but could record the timing of metamorphism associated with the sillimanite growth. More geochronology is required to better constrain the Nordmannvik Nappe origin.

7.2 The Baltican margin of northern Norway at the onset of the Caledonian Orogeny

The structures and metamorphic conditions indicate in-sequence nappe stacking of the RNC during S2 shearing. Considering the lack of typical suture rocks of oceanic affinity anywhere between the RNC and Baltica, a simple block model can be constructed for a paleogeographic reconstruction of the tectonostratigraphy showing the relative position of the nappes immediately prior to stacking (Fig. 14A). Irrespective of whether the complex polyphase KNC rocks are exotic or formed at the edge of Baltica (e.g. Corfu et al., 2007; Kirkland et al., 2007b, 2008; Gee et al., 2017), they must have been positioned at the edge of Baltica immediately prior to continental collision and crustal thickening because there are no Caledonian suture rocks tectonostratigraphically below them (Fig. 14A). The presence of variably sheared conglomerates at the base of the Vaddas Nappe that often directly overlie the KNC, and which include clasts resembling KNC rocks (Fig. 4D; Lindahl et al., 2005), indicate that at least the upper Vaddas Nappe rocks were probably deposited on a KNC-type basement during the late Ordovician/early Silurian (Binns and Gayer, 1980; Fig. 14A). The similarity of the metasediments in the lower Kåfjord Nappe and the Vaddas Nappe suggests they represent a similar but stratigraphically higher, or more distal equivalent (e.g. Fig. 14A). The preservation of the early heating event in the lower Kåfjord Nappe garnet cores indicates the rocks were at a higher stratigraphic level with respect to the Nordmannvik during the early Silurian, similar to, or slightly shallower than the depth of gabbro intrusion into the Vaddas Nappe. The upper Kåfjord rocks, displaying an age of 440 Ma for anatexis (Dangla et al., 1978) probably represent strongly sheared Nordmannvik-derived rocks. The tectonostratigraphic position of the Nordmannvik paragneisses and their likely older depositional age suggests they could also have been part of a more outboard depositional basement to the Vaddas/Kåfjord metasediments.

The marked decrease in metamorphic grade between the Nordmannvik (amphibolite-granulite facies) and Lyngsfjellet (greenschist-low amphibolite facies) nappes suggests that the Lyngsfjellet Nappe was not thrust in-sequence over the Nordmannvik nappe, and also that it did not reach the same depths as the RNC or KNC. Based on its current

position the Lyngsfjellet Nappe must have been somewhere outboard of the Nordmannvik Nappe rocks, with the overlying Nakkedal and Tromsø nappes representing more exotic elements (Corfu et al., 2003; Janák et al., 2012; Augland et al., 2014). The ophiolitic rocks in the Lyngsfjellet Nappe are interpreted to have formed in an incipient arc setting during the Early Ordovician (Kvassnes et al., 2004; Augland et al., 2014), although it should be noted that arc-like signatures may be inherited during subduction-related modification of mantle rocks (e.g. Moores et al., 2000) and the history of the Lyngen ophiolite is still unresolved.

7.3 The Caledonian evolution of the RNC

Any tectonic model relating to the Caledonian evolution of the RNC needs to explain the following: 1) the lack of typical suture rocks between the RNC and Baltica and the presence of an ophiolite on top of the RNC, 2) Ordovician/early Silurian deposition of Vaddas and (probably) Kåfjord volcanic sediments likely on a KNC basement, 3) intrusion of tholeiitic gabbro at ~23-30 km depth into almost synchronously deposited sediments (Vaddas), 3) the anticlockwise P-T path formed by early Caledonian heating and subsequent cooling and burial, and 5) the metamorphic gradient through the nappes during S2 shearing. In particular, the combination of rapid Ordovician/early Silurian volcaniclastic sedimentation, followed by early Silurian migmatitisation at deeper levels and coeval gabbro intrusions at higher crustal levels need a tectonic explanation. Three tectonic scenarios offer likely explanations for this evolution: 1) subduction of a spreading ridge, 2) spreading in an incipient back-arc basin followed by continental collision, and 3) slab-break off at the onset of continental collision.

(1) Ridge subduction, proposed by Northrup, (1997) and Corfu et al., (2006), explains the apparent coeval deposition of volcaniclastic sediments and tholeiitic mafic intrusions. However, the effect of ridge subduction on magmatism is usually very localized (e.g. Lomize and Luchitskaya, 2012). Ridge subduction does not explain the widespread nature of the early Silurian mafic magmatism several hundreds of kilometer along strike of the Caledonian orogen. (2) Deposition of volcaniclastic sediments in a continental basin and tholeiitic mafic magmatism is often indicative of an extensional setting such as

an incipient continental back-arc basin (e.g. Pedersen et al., 1992; Kirkland et al., 2005). Magmatic underplating of mafic magmas documented by the gabbro intrusions is likely to have provided heat for migmatisation in the Nordmannvik Nappe that occurred synchronously with the intrusions. Based on the tectonostratigraphy, a continental back arc basin with a KNC basement requires Ordovician/early Silurian eastward subduction of the Laurentia plate beneath Baltica (e.g. Andréasson et al., 2003). The main limitations of this model include: 1) gabbro intrusion depth into the Vaddas sediments requires that they were rapidly buried to at least 20 km depth in the back-arc basin, and 2) the timing of the anticlockwise P-T path suggests an extremely rapid switch from an extensional back-arc environment to a compressional crustal thickening, and structures in the migmatites indicate that they were initially deformed during collision while still partially molten, and 3) given the paleogeography, the position of an RNC back arc requires eastward subduction, which so far has not been described.

(3) Slab-break off at the onset of continental collision (e.g. Davies and von Blanckenburg, 1995; Zhu et al., 2015) is characterized by: 1) magmatism as a result of enhanced heat input from the rising asthenosphere, 2) magmatism and metamorphism near the suture and center of the orogen, and 3) melts emplaced in both extensional and compressive environments (Davies and von Blanckenburg, 1995). All three of these characteristics fit well with the RNC record. In such a model, Vaddas/Kåfjord sediments would have been deposited in a shallow sea between Baltica and Laurentia on the extended Baltica continental margin (Fig. 14B, step 1). Rapid accretion and burial of the margin and overlying sediments to depths > 20 km followed, with subsequent slab break-off facilitating rising of the asthenosphere providing a heat and mafic magma source for migmatisation of the Nordmannvik rocks and intrusion of tholeiitic gabbro bodies into the RNC rocks in a compressional setting (Fig. 14B, step 2). The presence of sagvandites (carbonate-orthopyroxenites formed by metasomatism of peridotite; Schreyer et al., 1972; Ohnmacht, 1974) in the Nordmannvik Nappe is also consistent with these rocks having come into contact with the lithospheric mantle. The partial melting of the pelitic rocks in combination with intercalated calc-silicate rocks provided the CO_2 and H_2O fluids for the sagvandite metasomatism of the mantle rocks, which were incorporated as mantle slices

into the Nordmannvik Nappe during thrusting (Figure 14B, step 3). Initial deformation associated with stacking of the Nordmannvik Nappe over the Kåfjord and Vaddas metasediments occurred while the Nordmannvik was still partially molten. Nappe stacking continued and facilitated shortening during continental collision (Fig. 14B, step 4).

The generally pervasive nature of the S2 deformation and the consistency of transport direction in the internal parts of the nappes with their boundaries provide evidence for large-scale distributed strain during lower crustal S2 nappe stacking. Since thrusting in the RNC is in sequence, estimated relative pressure differences between the nappes could result from slight temporal and spatial variation in deformation and metamorphism. While the rocks generally display similar temperatures (within error) during nappe thrusting, pressures in the RNC increase downwards (Fig. 13A). This increase in pressure downwards could have resulted from juxtaposition of the nappes facilitated by underthrusting of lower nappes below upper nappes. For example, the higher S2 pressures in the Vaddas and Kåfjord nappes relative to the Nordmannvik Nappe suggest that they underthrust the Nordmannvik Nappe during crustal thickening.

8 Strain localization and nappe stacking in continental collision zones

Caledonian nappe stacking in the RNC of northern Norway initially involved deeply buried (~30-35 km), hot (760-790°C), partially molten crustal rocks of the Nordmannvik Nappe. This is in contrast with anorthositic and granulitic Baltica crust in the Western Gneiss Region (WGR) and Lofoten further south in Norway. These crustal segments were subducted to depths >100 km with little internal deformation (Engvik et al., 2000; Hacker et al., 2010; Froitzheim et al., 2016). The anorthositic and granulitic rocks are not fertile or require large amounts of H_2O for partial melting. On the other hand, the Nordmannvik rocks are fertile and show extensive Caledonian partial melting at high pressures, associated with subduction of continental crust. This suggests that partial melts present in subducting rocks could play a role in controlling the style of deformation in continental collision zones: rock strength is significantly decreased even with melt

fractions as low as ~7%, and melt-bearing systems may facilitate strain localization (e.g. Rosenberg et al., 2005; Cavalcante et al., 2016).

In northern Norway, the fertile Nordmannvik rocks, which formed part of the pre-Caledonian outer Baltica margin, are significantly different in composition to the dry, strong Baltica basement of the WGR and Lofoten. Partial melting in the fertile subducted northern Norwegian Baltica margin led to strain localization, which facilitated the dismembering of the subducting rocks (Fig. 14B, steps 2 and 3). The partial melting is likely to be the critical weakening mechanism that prevented subduction of the hot bouyant Nordmannvik and RNC crust by initiating nappe stacking and thrusting instead. This is supported by the P-T path displayed by the Nordmannvik Nappe, which shows mainly cooling and that its depth did not increase between S1 migmatization and S2 shearing. This implies that its partially molten state made it too buoyant to reach greater depths during S2 shearing. The age of UHP metamorphism in Lofoten and WGR (c. 400 Ma; Hacker et al., 2010; Froitzheim et al., 2016) indicates that stronger Baltican crustal rocks continued to subduct beneath Laurentia for at least another ~30 Ma. The contrasts between dry and non-fertile (WGR, Lofoten) versus fertile and "wet" lithologies (RNC) highlight a major difference in the style of continental subduction and nappe stacking between different tectonostratigraphic levels. The response of the lithology to the metamorphic conditions exerts a key control on the strength of the subducted continental rocks and in this way the integrity of the down-going rocks.

9 Conclusions

Five main conclusions can be made. 1) In northern Norway the KNC and RNC probably comprised an extended Baltica continental edge immediately prior to nappe stacking. 2) The Caledonian evolution of the rocks records a continuous sequence of events including: (i) late Ordovician/early Silurian volcaniclastic sedimentation in the Vaddas and Kåfjord nappes, (ii) an anticlockwise P-T path with early high temperature partial melting in the Nordmannvik and mafic magmatism in the Vaddas, Kåfjord and Nordmannvik nappes at ~443-435 Ma, followed by (iii) amphibolite-facies shearing and nappe stacking recorded at ~437-427 Ma along the RNC-KNC boundary. 3) Mid-crustal high-temperature

metamorphism concurrent with mafic magmatism in a compressional setting in the RNC rocks is best explained by magma underplating, possibly caused by slab break-off during early collisional stages. 4) The partially molten and hot nature of the RNC rocks probably inhibited their subduction in northern Norway and led to weakening, strain localization and initiation of nappe stacking.

References

Andresen, A, and Bergh, S., 1985. Stratigraphy and tectonometamorphic evolution of the Ordovician-Silurian Balsfjord Group, Lyngen Nappe, north Norwegian Caledonides, The Caledonian Orogen – Scandinavia and related areas Part 1, 579-592.

Andresen, A., 1988. Caledonian terranes of northern Norway and their characteristics. Trabajos de Geologia, University of Oviedo, 17, 103-117.

Andresen, A., and Steltenpohl, M.G., 1994. Evidence for ophiolite obduction, terrance accretion and polyorogenic evolution of the north Scandinavian Caledonides, Tectonophysics, 231, 59-70.

Andréasson, P.G., Gee, D.G., Whitehouse, M.J., and Schöberg, H., 2003. Subduction-flip during Iapetus Ocean closure and Baltica-Laurentia collision, Scandinavian Caledonides, Terra Nova, 15, 362-369.

Augland, L.E., Andresen, A., Gasser, D., and Steltenpohl, G., 2014. Early Ordovician to Silurian evolution of exotic terranes in the Scandinavian Caledonides of the Ofoten-Troms area – terrane characterization and correlation based on new U-Pb zircon ages and Lu-Hf isotopic data, Geological Society, London, Special Publications, 390, 655-678

Beaumont, C., Nguyen, M.H., Jamieson, R.A., and Ellis, S., 2006. Crustal flow modes in large hot orogens, Geological Society, London, Special Publications, 268, 91-145.

Binns, R.E., 1978. Caledonian nappe correlation and orogenic history in Scandinavia north of lat 67 °N, Geological Society of America Bulletin, 89, 1475-1490.

Binns, R.E., and Gayer, R.A., 1980. Silurian or Upper Ordovician fossils of Goulasjavri, Norway. Nature, 284, 53-54.

Caddick, M.J., Konopasek, J., and Thompson, A.B., 2010. Preservation of garnet growth zoning and the duration of prograde metamorphism, Journal of Petrology, 51, 2327-2347.

Cavalcante, G.C.G., Viegas, G., Archanjo, C.J., and da Silva, M, E., 2016. The influence of partial melting and melt migration on the rheology of the continental crust, Journal of Geodynamics, 101, 186-199.

Cherniak, D.J., 1993. Lead diffusion in titanite and preliminary results on the effects of radiation damage on Pb transport, Chemical Geology, 125, 219-232.

Chopin, C., 2003. Ultrahigh-pressure metamorphism: tracing continental crust into the mantle, Earth and Planetary Science Letters, 212, 1-14.

Coggon, R., and Holland, T.J.B., 2002, Mixing properties of phengitic micas and revise garnet-phengite thermobarometers, Journal of Metamorphic Geology, 20, 683-696.

Connolly, J.A.D., 2005, Computation of phase equilibria by linear programming: a tool for geodynamic modelling and its application to subduction zone decarbonation. Earth and Planetary Science Letters, 236,524–541.

Corfu, F., Ravna, E.J.K., and Kullerud, K., 2003. A late Ordovician U-Pb age for the Tromsø Nappe eclogites, Uppermost Allcohton of the Scandinavian Caledonides, Contributions to Mineralogy and Petrology, 145, 502-513.

Corfu, F., Torsvik, T.H., Andersen, T.B., Ashwal, L.D., Ramsay, D.M., and Roberts, R.J., 2006. Early Silurian mafic-ultramafic and granitic plutonism in comtemporaneous flysch, northern Norway: U-Pb ages and regional significance, Journal of the Geological Society, 163, 291-301.

Corfu, F., Roberts, R.J., Torsvik, T.H., Ashwal, L.D., Ramsay, D.M., 2007. Peri-Gondwanan elements in the Caledonian nappes of Finnmark, northern Norway: implications for the paleogeographic framework of the Scandianvian Caledonides, 307, 434-458.

Corfu, F., Gerber, M., Andersen, T.B., Torsvik, T.H., and Ashwal, L.D., 2011. Age and significance of Grenvillian and Silurian orogenic events in the Finnmarkian Caledonides, northern Norway, Canadian Journal of Earth Sciences, 48, 419-440.

Corfu, F., Gasser, D., and Chew, D.M., 2014. New perspectives on the Caledonides of Scandinavia and related areas: introduction, Geological Society, London, Special Publications, 390. 1-8.

Dangla, P., Damange, J.C., Ploquin, A., Quarnardel, J.M., and Sonet, J., 1978. Donn'es geochronologiques sur les Caledonides Scandinaves septentrionates (Troms, Norway du Nord), C.r. Acad. Sci. Paris, 286 D, 1.653-1.656.

Davies, J.H., and von Blanckenburg, F., 1995. Slab breakoff: A model of the lithosphere detachment and its test in the magmatism and deformation of collisional orogens, Earth and Planetary Science Letters, 129, 85-102.

Elvevold, S., 1987. Petrologiske undersøkelse av Kaledonske bergater i Takvatnområdet, Troms, Masteroppgave, Universitetet i Tromsø.

Elvevold, S., and Andersen, T., 1993. Fluid evolution during metamorphism at increasing pressure: carbonic- and nitrogen-bearing fluid inclusions in granulites from Øksfjord, north Norwegian Caledonides, Contributions to Mineralogy and Petrology, 114, 236-246.

Elvevold, S., Reginiussen, H., Krogh, E.J., and Bjørklund, F., 1994. Reworking of deep-seated gabbros and associated contact metamorphosed paragneisses in the southeastern part of the Seiland Igneous Province, northern Norway, Journal of Metamorphic Geology, 12, 539–556.

Engvik, A.K., Austrrheim, H., Andersen, T.B., 2000. Structural, mineralogical and petrophysical effects on deep crustal rocks of fluid-limited polymetamorphism, Western Gneiss Region, Norway, Journal of the Geological Society, 157, 121-134.

Escher, A., Masson, H., and Steck, A., 1993. Nappe geometry in the Western Swiss Alps, Journal of Structural Geology, 15, 501-509.

Escher, A., and Beaumont, C., 1997. Formation, burial and exhumation of basement nappes at crustal scale: a geometric model based on the Western Swiss-Italian Alps, Journal of Structural Geology, 19, 955-974.

Froitzheim, N., Miladinova, I., Janák, M., Kullerud, K., Ravna, E.K., Majka, J., Fonseca, R.O.C., and Münker, C., 2016. Devonian subduction and syncollisional exhumation of continental crust in Lofoten, Norway, Geology, 44, 223-226.

Frost, B.R., Chamberlain, K.R., and Schumacher, J.C., 2001. Sphene (titanite): phase relations and role as a geochronometer, Chemical Geology, 172, 131-148.

Gasser, D., Jerabek, P., Faber, C. Stünitz, H., Menegon, L., Corfu, F., Erambert, M., and Whitehouse, M.J., 2013. Behaviour of geochronometers and timing of the metamorphic reactions during deformation at lower crustal conditions: phase equilibrium modeling and U-Pb dating of zircon, monazite, rutile and titanite from the Kalak Nappe Complex, northern Norway, Journal of Metamorphic Geology, 33, 513-534.

Gayer, R.A., and Roberts, J.D., 1973. Stratigrahic review of the Finnmark Caledonides, with possible tectonic implications, Proceedings of the Geologists' Association, 84, 405-428.

Gee., D.G., Juhlin, C., Pascal, C., Robinson, P., 2010. Collisional Orogeny in the Scandinavian Caledonides (COSC), GFF: Journal of the Geological Society of Sweden, 132, 29-44

Gee, D.G., Andréasson, P.G., Li, Y., and Krill, A., 2017. Baltoscandian margin, Sveconorwegian crust, lost by subduction during Caledonian collisional orogeny, GFF: Journal of the Geological Society of Sweden, 139, 36-51.

Gerya, T.V., and Meilick, F.I., 2010. Geodynamic regimes of subduction under an active margin: effects of rheological weakening by fluids and melts, Journal of Metamorphic Geology, 29, 7-31.
Getsinger, A.J., Hirth, G., Stünitz, H., and Georgen, E.T., 2013. Influence of water on rheology and strain localization in the lower continental crust, Geochemistry, Geophysics, Geosystems, 14, 2247-2264.
Hacker, B.R., Andersen, T.B., Johnston, S., Kylander-Clark, A.R.C., Peterman, E.M., Walsh, E.O., and Young, D., 2010. High-temperature deformation during continental-margin subduction and exhumation: The ultra-high pressure Western Gneiss Region of Norway, Tectonophysics, 480, 149-171.
Holland, T.J.B. & Powell, R., 1998, An internally consistent thermodynamic data set for phases of petrological interest. Journal of Metamorphic Geology, 16, 309–343.
Holland, T., and Powell, R., 2001, Calculation of phase relations involving haplogranitic melts using an internally consistent thermodynamic dataset, Journal of Petrology, 42, 673-683.
Hollister, L.S., and Crawford, M.L., 1986. Melt-enhanced deformation: A major tectonic process, Geology, 14, 558-561.
Hoskin, P.W.O., and Schaltegger, U., 2003. The composition of zircon and igneous and metamorphic petrogenesis, Reviews in Mineralogy and Geochemistry, 53, 27-62.
Janák, M., Ravna, E.J.K., Kullerud, K., 2012. Constraining peak P-T conditions in UHP eclogites: calculated phase equilibria in kyanite- and phengite-bearing eclogite of the Tromsø Nappe, Norway, Journal of Metamorphic Petrology, 30, 377-396.
Jeřábek, P., Lexa, O., Schulmann, K., and Plašienka, D., 2012. Inverse ductile thinning via lower crustal flow and fold-induced doming in the West Carpathian Eo-Alpine collisional wedge, Tectonics, 31, TC5002.
Kirkland, C.L., Daly, J.S., and Whitehouse, M.J., 2005. Early Silurian magmatism and the Scandian evolution of the Kalak Nappe Complex, Arctic Norway, Journal of the Geological Society, 162, 985-1003.
Kirkland, C.L., Daly, J.S., and Whitehouse, M.J., 2006. Granitic magmatism of Grenvillian and late Neoproterozoic age in Finnmark, Arctic Norway – constraining pre-Scandian deformation in the Kalak Nappe Complex, Precambrian Research, 145, 24-52.
Kirkland, C.L., Daly, J.S., Eide, E.A., and Whitehouse, M.J., 2007a. Tectonic evolution of the arctic Norwegian Caledonides from a texturally- and structurally- constrained multi-isotopic (Ar-Ar. Rb-Sr, Sm-Nd, U-Pb) study, American Journal of Science, 307, 459-526.
Kirkland, C.L., Daly, J.S., and Whitehouse, M.J., 2007b. Provenance and terrane evolution of the Kalak Nappe Complex, Norwegian Caledonides: implications for Neoproterozoic paleogeography and tectonics, The Journal of Geology, 115, 21-41.
Kirkland, C.L., Daly, J.S., and Whitehouse, M.J., 2008. Basement-cover relationships of the Kalak Nappe Complex, Arctic Norwegian Caledonides and constraints on Neoproterozoic terrane assembly in the North Atlantic region, Precambrian Research, 160, 245-276.
Kirkland, CL., MacGabhann, B.A., Kirkland, B.L., and Daly, J.S., 2016. Cryptic disc structures resembling Ediacaran discoidal fossils from the lower Silurian Hellefjord Schist, Arctic Norway, PloS ONE, 11, e0164071.
Kohn, M.J., Corrie, S.L., Markley, C., 2015. The fall and rise of metamorphic zircon. American Mineralogist, 100, 897–908.
Kohn, M.J., 2017. Titanite petrochronology, Reviews in Mineralogy and Geochemistry, 83, 419-441.
Kvassnes, A.J.S., Strand, A.H., Moen-Eikeland, H., and Pedersen, R.B., 2004. The Lyngen Gabbro: the lower crust of an Ordovician Incipient arc, Contributions to Mineralogy and Petrology, 148, 358-379.
Labrousse, L., Hetenyi, G., Raimbourg, H., Jolivet, L., and Andersen, T.B., 2010. Initiation of crustal-scale thrusts triggered by metamorphic reactions at depth: Insights from a comparison between the Himalayas and Scandinavian Caledonides, Tectonics, 29, TC5002.

Larson, S.A., and Berglund, J., 1992. A chronological subdivision of the Transscandinavian Igneous Belt – three magmatic episodes? Geologiska Foreningen i Stockholm Forhandlingar, 114, 459-461.

Lindahl, I., Stevens, B.P.J., and Zwaan, K.B., 2005. The geology of the Vaddas area, Troms: a key to our understanding of the Upper Allochton in the Caledonides of northern Norway, NGU Bulletin, 445, 5-43.

Lindstrøm, M., and Andresen, A., 1992. Early Caledonian high-grade metamorphism within exotic terranes of the Troms Caledonides? Norsk Geologisk Tidsskrift, 72, 375-379.

Lomize, M.G., and Luchitskaya, M.V., 2012. Subduction of spreading ridges as a factor in the evolution of continental margins, Geotectonics, 46, 47-68.

Melezhik, V.A., Kuznetsov, A.B., Pokrovsky, B.G., Solli, A., Gorokhov, I.M., Fallick, A.E., Lindahl, I., Konstantinova, G.V., and Melnikov, N.N., 2014. Chemostratigraphic insight into deposition of the Melkedalen Marble, Narvik Nappe Complex, North-Central Norwegian Caledonides, Norwegian Journal of Geology, 94, 35-52.

Moores, E.M., Kellogg, L.H., and Dilek, Y., 2000. Tethyan ophiolites, mantle convection, and tectonic "historical contingency"; a resolution of the "ophiolite conundrum," in Dilek, Y., Moores, E.M., Elthon, D., and Nicolas, A., eds., Ophiolites and Oceanic Crust: New Insights from Field Studies and the Ocean Drilling Program: Geological Society of America Special Paper, 349, 3–12.

Northrup, C.J., 1997. Timing structural assembly, metamorphism, and cooling of the Caledonian Nappes in the Ofoten-Efjord area, North Norway: tectonic insights from U-Pb and $^{40}Ar/^{39}Ar$ geochronology, Journal of Geology, 105, 565-582.

Ohnmacht, W., 1974. Petrogenesis of carbonate-orthopyroxenites (Sagvandites) and related rocks from Troms, Northern Norway, Journal of Petrology, 15, 303-324.

Palin, R.M., Weller, O.M., Waters, D.J., and Dyck, B., 2016. Quantifying geological uncertainty in metamorphic phase equilibria modelling; a Monte Carlo assessment and implications for tectonic interpretations, Geoscience Frontiers, 7, 591-607.

Pedersen, R.B., Bruton, D.L., and Furnes, H., 1992. Ordovician faunas, island arcs and ophiolites in the Scandinavian Caledonides, Terra Nova, 4, 217-222.

Ramsay, D.M., Sturt, B.A., Zwaan, K.B., and Roberts, D., 1985. Caledonides of Northern Norway, in Gee, D.G., and Sturt, B.A. (eds), The Caledonian Orogen – Scandinavia and Related areas: New York, Wiley, 163-184.

Rice, A.H.N., 1998. Stretching lineations and structural evolution of the Kalak Nappe Complex (Middle Allochton) in the Repparfjord-Fægfjord area, Finnmark, northern Norway, Norsk Geologisk Tidsskrift, 78, 277-289.

Rice, A.H.N., 2014. Restoration of the external Scandinavian Caledonides, Finnmark, North Norway, Geological Society of London, Special Publications, 390, 271-299.

Roberts, D., 1973. Geologisk kart over Norge, berggrunnskart,. Hammerfest 1:250 000, Norges Geologiske Undersøkelse.

Roberts, D., and Sturt, B.A., 1980. Caledonian deformation in Norway, Journal of the Geological Society, 137, 241-250.

Roberts, D., and Gee, D.G., 1985. An introduction to the structure of the Scandinavian Caledonides. In: Gee, D.G., and Sturt, B.A. (eds), The Caledonian Orogen – Scandinavia and Related areas, Wiley, Chichester, 55-68.

Robins, B., 1998. The mode of emplacement of the Honningsvåg Intrusive Suite, Magerøya, northern Norway., Geological Magazine, 135, 231-244.

Rosenberg, C.L., and Handy, M.R., 2005. Experimental deformation of partially melted granite revisited: implications for the continental crust, Journal of Metamorphic Geology, 23, 19-28.

Schreyer, W., Ohnmacht, W., and Mannchen, J., 1972. Carbonate-orthopyroxenites (sagvandites) from Troms, northern Norway, Lithos, 5, 345-364.

Schulte-Pelkum, V., Monslave, G., Sheehan, A., Pandey, M.R., Sapkota, S., Bilham, R., and Wu, F., 2005. Imaging the Indian subcontinent beneath the Himalaya, Nature, 435, 1222-1225.
Spencer, K.J., Hacker, B.R., Kylander-Clark, A.R.C., Andersen, T.B., Cottle, J.M., Stearns, M.A., Poletti, J.E., Seward, G.G.E., 2013. Campaign-style titanite U–Pb dating by laser-ablation ICP: Implications for crustal flow, phase transformations and titanite closure. Chemical Geology 341, 84–101.
Spengler, D., Brueckner, H.K., Roermund, H.L.M., Drury, M.R., and Mason, P.R.D., 2009. Long-lived, cold burial of Baltica to 200 km depth, Earth and Planetary Science Letters, 281, 27-35.
Steltenpohl, M.G., Andresen, A., and Tull, J.F., 1990. Lithostratigraphic correlation of the Salangen (Ofoten) and Balsfjord (Troms) Groups: evidence for the post-Finnmarkian unconformity, north Norwegian Caledonides, American Journal of Science, 303, 149-185.
Stephens, M.B., and Gee, D.G., 1989. Terranes and polyphase accretionary history in the Scandinavian Caledonides. In: Dallmeyer, R.D. (ed.) Terranes in the Circum-Atlantic Paleozoic Orogens, Geological Society of America Special Papers, 230, 17-30.
Streule, M.J., Strachan, R.A., Searle, M.P., and Law, R.D., 2010. Comparing Tibet-Himalayan and Caledonian crustal architecture, evolution and mountain building processes, Geological Society, London, Special Publications, 335, 207-232.
Tucker, R.D., Boyd, R.D., and Barnes, S.J., 1990. A U-Pb zircon age for the Råna intrusion, N. Norway: new evidence of basic magmatism in the Scandinavian Caledonides in Early Silurian time, Norsk Geologisk Tidsskrift, 70, 229-239.
Tucker, R.D., Robinson, P., Solli, A., Gee, D.G., Thorsnes, T., Krogh, T.E., Nordgulen, O., and Bickford, M.E., 2004. Thrusting and extension in the Scandian hinterland, Norway: New U-Pb ages and tectonostratigraphic evidence, American Journal of Science, 304, 477-532.
Vaasjoki M., and Sipilä, P., 2001. U-Pb isotope determinations on baddeleyite and zircon from the Halti-Ridnitsohkka intrusion in Finnish Lapland: a further constraint on the Caledonide evolution, Geological Society of Finalnd, Special Paper, 33, 247-253.
Wakabayashi, J., 2004. Tectonic mechanisms associated with P-T paths of regional metamorphism: alternatives to singe-cycle thrusting and heating, Tectonophysics, 392, 193-218.
Whitney, D.L., and Evans, B.W., 2010. Abbreviations for names of rock-forming minerals, American Mineralogist, 95, 185-187.
Zhao, Z., Mo, X., Dilek, Y., Niu, Y., DePaolo, D.J., Robinson, P., Zhu, D., Sun, C., Dong, G., Zhou, S., Luo, Z., and Hou, Z., 2009. Geochemical and Sr-Nd-Pb-O isotopic compositions of the post-collisional ultrapotassic magmatism in SW Tibet: Petrogenesis and implications for India intra-continental subduction beneath southern Tibet, Lithos, 113, 190-212
Zhu, D-C., Wang, Q., Zhao. Z-D., Chung, S-L-. Cawood, P.A., Niu, Y., Liu, S-A., Wu, F-Y., and Mo, X-X-. 2015. Magmatic record of India-Asia collision, Scientific Reports, 5, 1-8.
Zwaan, K.B., and Roberts, D., 1978. Tectonostratigraphic succession and development of Finnmarkian Nappe sequence, North Norway, Norges Geologiske Undersøkelse, 343, 53-71
Zwaan, K.B., 1988. Nordreisa, berggrunnsgeologisk kart – M 1:250 000. Norges geologiske unerdsøkelse.

Figure Captions

Figure 1: A) Simplified map of the Scandinavian Caledonides and their inferred palaeotectonic origin, modified from Gee et al. (2010). LNC = Lyngsfjellet Nappe

Complex, WGR=Western Gneiss Region, NNC=Narvik Nappe Complex, KNC=Kalak Nappe Complex, RNC=Reisa Nappe Complex. B) Map showing the extent of the Reisa Nappe Complex in northern Norway, based on Zwaan (1988) and own correlations. The Vaddas, Kåfjord and Nordmannvik nappes are shown in colour. The study area is denoted by the black box (Fig. 2).

Figure 2: Structural map, stereonets and cross sections from the study area. Sample sites for petrological and geochronological samples are indicated. Structures are shown on equal area lower hemisphere stereographic projections. A) Structures in the RNC on northern and western Arnøya. B) Structures in the RNC on southernmost Arnøya. C) Structures in the KNC on Uløya; poles to S2 plot on a great circle (dashed line), the pole of which (black box) defines a fold hinge parallel to plotted stretching lineations. D) Structures in the RNC on Uløya. E) Structures from the Nordmannvik Nappe on the eastern coast of Lyngen. F) Structures in the Vaddas Nappe on the eastern side of Reisafjord; poles to foliation define a folding event with the fold hinge (black box) parallel to the L2 stretching lineation and measured open fold axes. Cross sections are shown at the bottom of the figure. The density of red lines in the cross sections from Arnøya to Eide (A-B) and from Lyngen to Sørkjosen (C-D) corresponds to the intensity of ductile deformation within and along boundaries between individual nappes. Caledonian foliations are shown in red, whereas black are possibly older.

Figure 3: Representative tectonostratigraphy of the Reisa Nappe Complex from west of Lyngen (Lyngseidet) to Straumfjord and Kvænangen (east) showing the location of major structures and relative thickness and spatial variation of tectonic units. Based on Zwaan (1988), Lindahl et al., (2005) and own work. Tectonostratigraphic position of the investigated samples is indicated.

Figure 4: Field photographs and photomicrographs from Vaddas and Kåfjord nappes. Co-ordinates for sample sites are given in Table 1. A) KNC paragneiss with visible (sheared) leucosome from 30 m below the Vaddas-KNC boundary shear zone at site UL248. B) The Vaddas-KNC boundary mylonite at site UL248. C) Photomicrograph of

sample UL248 showing the edge of a K-feldspar porphyroclast, garnet with a rutile inclusion, and matrix with biotite and titanite visible. D) Outcrop of sheared metaconglomerate from the base of the Vaddas Nappe on Uløya at N69.89326°, E20.55713° with mostly rounded quartzite clasts in a pelitic matrix of biotite and garnet. E) Typical strongly sheared garnet-mica schist and amphibolite in the Vaddas Nappe at N69.89326°, E20.55456° (Uløya). F) Photomicrograph of Vaddas Nappe sample AR71 showing sheared garnet (top-to-SE shear sense), and muscovite fish, biotite and rutile in the matrix. G) A sheared calc-silicate lens (top-to-SE shear sense) in typical garnet-zoisite-biotite schist from the lower Kåfjord Nappe at N69.85701°, E20.53317°. H) Photomicrograph of garnet in Kåfjord Nappe sample AR153 showing distinctive core and rim structure with chlorite inclusions in garnet cores and rutile in the matrix. I) Photomicrograph of Kåfjord Nappe sample AR153 showing garnet porphyblasts in a matrix with S2 foliation defined by zoisite, biotite and muscovite. An ilmenite inclusion in garnet is also shown.

Figure 5: Field photographs and photomicrographs from the Nordmannvik Nappe. A) Photograph of Nordmannvik mylonite (solid-state deformed (S2) migmatite) at sample site AR26 near the Nordmannvik-Kåfjord boundary. B) Photomicrograph of sample AR26 showing garnet porphyroblasts with sillimanite inclusions in a matrix with a strong S2 foliation defined by biotite, kyanite and muscovite. C) Photograph showing a lens-shaped domain in the Nordmannvik Nappe on Uløya at N69.84046°, E20.51852° with an older S1 migmatitic foliation overprinted and sheared by solid-state S2 mylonitic foliation. D) Photograph of Nordmannvik migmatite at site AR23 showing the folded S1 migmatitic foliation (Caledonian fold geometry) with melt segregations in an axial planar orientation (white arrow; parallel to S2). E) Photograph of Nordmannvik migmatite at sample site AR25b showing a high volume of leucosome and garnet- and biotite-rich melanosomes. F) Photomicrograph of sample AR25b showing a lack of S2 foliation, and kyanite and biotite along the edge of a leucosome segregation.

Figure 6: BSE images, compositional maps and garnet profiles from the Vaddas and Kåfjord nappes. A) Garnet from the KNC-Vaddas boundary, sample UL248, displays

strong zoning with defined core (Grt1) and rim (Grt2) zones and a transition zone between them. Pink grains in garnet rims are titanite. B) Garnet from the Vaddas Nappe, sample AR71, has a flat profile with occasional thin growth rims. C) Garnet from the Kåfjord Nappe, sample AR153, has a profile that shows some zoning, with mainly Grs and Sps contents displaying a difference between inclusion-rich cores and inclusion-poor rims.

Figure 7: Pseudosections describing metamorphism at the Kalak-Vaddas nappe boundary (sample UL248) and in the Vaddas (sample AR71) and Kåfjord (sample AR153). Resulting P-T estimates are derived from the composition of garnet and further constrained using feldspar, biotite and white mica where relevant. Estimates in the pseudosections are displayed as striped boxes. A) Garnet core (Grt1) growth conditions were estimated from the X_{Mg}, Grs and Sps contents of garnet cores. Isopleths for anorthite content are shown, and are in agreement with measured anorthite content in plagioclase cores. The pseudosection was calculated using the bulk composition determined from XRF analysis of the whole rock. B) S2 shearing conditions were estimated from X_{Mg}, Grs and Sps content correlating with measured garnet rims (Grt2). The estimate correlates well with anorthite content in plagioclase rims. The pseudosection was calculated using a bulk composition from which garnet cores were subtracted. C) Grs, Sps, and X_{Mg} contents in garnet give core and rim at slightly lower and higher pressures, respectively. Si (a.p.f.u) in muscovite was used to further constrain pressures. Retrogression to lower P-T is preserved in thin garnet rim compositions and ilmenite rims on rutile (white arrow). D) Grs, Sps and X_{Mg} contents in zoned garnets from the Kåfjord Nappe give a garnet core estimate at lower pressure conditions, and garnet rim estimate at higher pressure conditions. Chlorite and ilmenite inclusions in garnet cores are consistent with the garnet core estimate.

Figure 8: Raman spectra for a sillimanite inclusion from a garnet core in the Nordmannvik migmatite (sample AR25b).

Figure 9: BSE images and garnet profiles for Nordmannvik Nappe samples AR25b and AR26. A) Garnet in AR25b displays a profile with a steady increase in Alm, Grs and Sps contents and decrease in Py and X_{Mg} towards garnet rims. B) The garnet profile for the large garnet in sample AR26 displays a relatively flat profile with some compositional change towards the rims. An inclusion-free core, marked in grey on the profile and in white on the BSE image, shows slightly lower and more variable Grs content. C) The garnet profile for small garnets in sample AR26 shows a steady increase in Alm, Grs and Sps contents and steady decrease in Py and X_{Mg} contents towards the rims.

Figure 10: Pseudosections for the Nordmannvik Nappe. A) Measured garnet core and rim compositions for migmatite (AR25b) agree with modelled compositions that plot above the solidus. Garnet cores give an apparent estimate in the sillimanite stability field. Garnet rims record S1-related partial melting in the kyanite stability field. B) Measured compositions of garnet cores and rims for S2 mylonite (AR26) are shown. Garnet cores give an apparent estimate above the solidus in the sillimanite stability field (S1 melting). Garnet rims and small garnets give an estimate below the solidus for S2-shearing.

Figure 11: Age of partial melting and metamorphism in the Nordmannvik Nappe. A) CL images of zircon grains with single spot analyses. $^{206}Pb/^{238}U$ dates for spot analyses are as follows: 1) 440 ± 5 Ma, 2) 585 ± 8 Ma, 3) 439 ± 5 Ma, 4) 441 ± 5 Ma, 5) 1421 ± 16 Ma, 6) 443 ± 5 Ma, 7) 1547 ± 17 Ma. Note the presence of small, inherited cores. B) Terra-Wasserburg diagram for SIMS zircon analyses from the restite of sample AR25b. Inherited core analyses are shown as grey ellipses. C) Concordia diagram with age calculated for the young cluster of zircons in Fig. B. D) CL images of zircon grains from the sample with single spot analyses. $^{206}Pb/^{238}U$ dates for spot analyses are as follows: 8) 441 ± 5 Ma, 9) 440 ± 5 Ma, 10) 441 ± 5 Ma, 11) 435 ± 5 Ma, 12) 438 ± 5 Ma, 13) 434 ± 6 Ma. No inherited cores were observed in this sample. E) Terra-Wasserburg diagram and Concordia age for SIMS zircon analyses from the leucosome of sample AR25b. F) Calc-silicate and leucosome mixing zone at sample site A01. G) Close-up of calc-silicate and leucosome boundary showing titanite in a schlieren. H) Concordia diagram for U-Pb

TIMS analyses of titanites from a calc-silicate lens in the Nordmannvik Nappe (sample A01) with Concordia age calculated for 4 overlapping grains (in bold).

Figure 12: Ages related to intrusion and shearing in the Vaddas Nappe. A) Photograph of the sampled gabbroic pegmatite (sample Sk18b). Hammer head is 15 cm-long. B) CL images of single zircon grains with spot analyses shown. The spot analyses have the following $^{206}Pb/^{238}U$ dates: 1) 438 ± 2.5 Ma, 2) 438.2 ± 2.7 Ma, 3) 439.1 ± 2.5 Ma, and 4) 444.4 ± 2.8 Ma. C) Terra-Wasserburg diagram for SIMS zircon analysis from gabbroic pegmatite (sample SK18b) with Concordia age calculated showing the age of the Kågen gabbro intrusion into the Vaddas Nappe. D) Concordia diagram for U-Pb TIMS analyses of titanites from the Vaddas-Kalak boundary (sample UL248) with mean $^{206}Pb/^{238}U$ age calculated.

Figure 13: Summary of P-T conditions and timing for phase equilibrium modelling and geochronological results. A) P-T diagram comparing conditions of metamorphism for Pre-S1 garnet cores (striped boxes), S1 migmatisation (solid line box), apparent garnet core conditions in the Nordmannvik Nappe (dashed boxes), and S2 shearing (filled boxes) for all nappes. Estimated conditions for metamorphism in the KNC are shown in grey (Gasser et al., 2013). The intrusion conditions for the Kågen gabbro (brown box) are from Getsinger et al., (2013). Arrows show anticlockwise P-T paths for the Nordmannvik Nappe rocks and Vaddas/lower Kåfjord metasediments. B) Timing of magmatism and metamorphism comparing ages across the nappes of the RNC and placing them within a pre-Caledonian and Caledonian context. Titanite ages are shown as filled boxes and zircon ages as solid line boxes. Inferred and speculative ages are shown as dashed boxes.

Figure 14: Tectonic model for the Caledonian nappes in the study area. A) Block diagram showing the likely relative palaeogeography of the Baltica margin immediately prior Caledonian continental collision, with possible locations and relative timing of nappe shear boundaries shown in red. B) Schematic overview showing a possible Caledonian evolution for northern Norway. 1. The Pre-Caledonian Baltica continental margin with Late Ordovician/early Silurian deposition of the Vaddas/Kåfjord sediments

on the Baltica continental margin and subduction of Baltica oceanic crust beneath Laurentia. 2. Subduction of the Baltica continental edge causing burial of Nordmannvik, Kåfjord and Vaddas rocks followed by the break-off of Baltica oceanic slab causing rising of the asthenosphere and initiation of partial melting in the subducted Nordmannvik rocks and intial gabbro intrusion. 3. Detachment of the weak, partially molten Nordmannvik rocks from the continental lithosphere and initiation of nappe stacking and thrusting Nordmannvik over the lower Kåfjord metasediments. Incorporation of charnockites, continued gabbro intrusion (in a contractional setting) and thrusting of Kåfjord over Vaddas metasediments. 4. Relative emplacement of the RNC over the KNC with shearing along the KNC-Vaddas boundary between ~437-427 Ma, and nappe stacking within the KNC.

List of tables

Table 1: List of samples with rock types, sample sites and methods.

Table 2: Mineralogy for petrology samples.

Table 3: Representative garnet analyses showing re-calculated garnet compositions on the basis of 8 cations and 12 oxygens.

Table 4: Representative biotite, feldspar and white mica compositions.

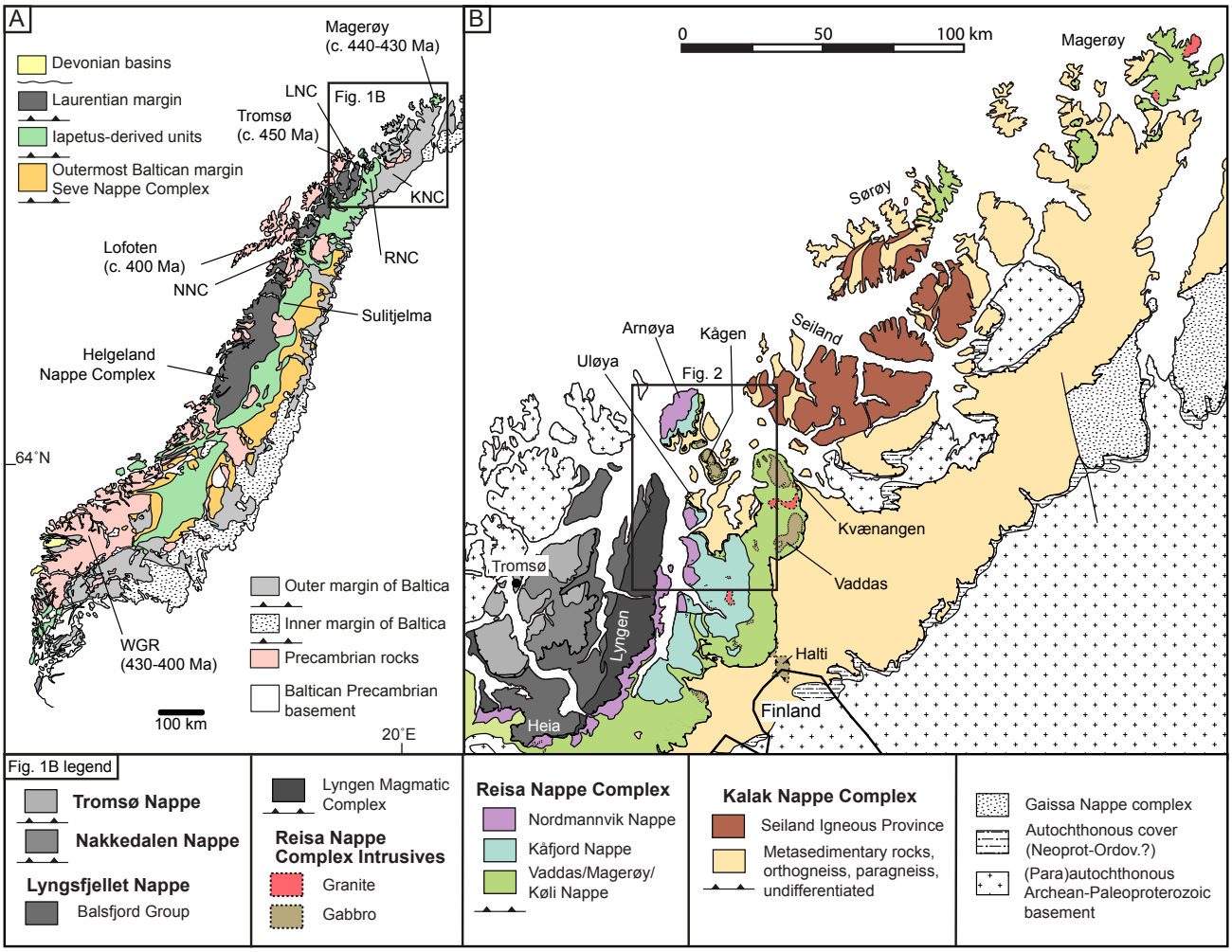
A
Devonian basins
Laurentian margin
Iapetus-derived units
Outermost Baltican margin
Seve Nappe Complex
Magerøy
(c. 440-430 Ma)
LNC
Fig. 1B
Tromsø
(c. 450 Ma)
KNC
RNC
Lofoten
(c. 400 Ma)
NNC
Sulitjelma
Helgeland
Nappe Complex
64˚N
WGR
(430-400 Ma)
100 km
20˚E
Outer margin of Baltica
Inner margin of Baltica
Precambrian rocks
Baltican Precambrian
basement
B
0
50
100 km
Magerøy
Sørøy
Seiland
Arnøya
Kågen
Uløya
Fig. 2
Kvænangen
Tromsø
Vaddas
Lyngen
Halti
Finland
Heia
Fig. 1B legend
Tromsø Nappe
Nakkedalen Nappe
Lyngsfjellet Nappe
Balsfjord Group
Lyngen Magmatic
Complex
Reisa Nappe
Complex Intrusives
Granite
Gabbro
Reisa Nappe Complex
Nordmannvik Nappe
Kåfjord Nappe
Vaddas/Magerøy/
Køli Nappe
Kalak Nappe Complex
Seiland Igneous Province
Metasedimentary rocks,
orthogneiss, paragneiss,
undifferentiated
Gaissa Nappe complex
Autochthonous cover
(Neoprot-Ordov.?)
(Para)autochthonous
Archean-Paleoproterozoic
basement

Fig. 1

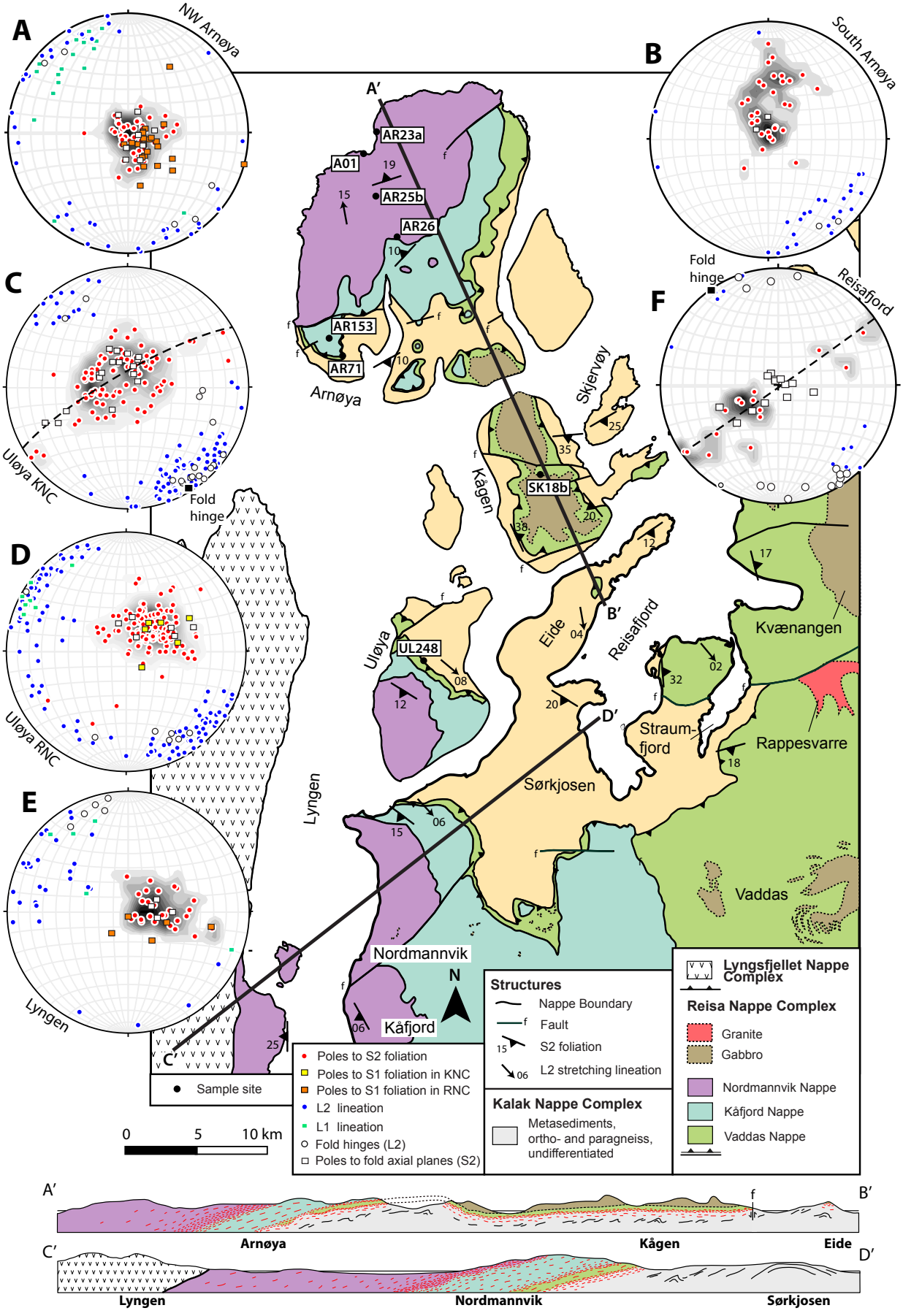
A
NW Arnøya
B
South Arnøya
C
Uløya KNC
D
Uløya RNC
E
Lyngen
F
Fold hinge
Reisafjord
A′
B′
C′
D′
AR23a
A01
19
15
AR25b
AR26
10
AR153
AR71
10
Arnøya
Skjervøy
25
35
Kågen
SK18b
38
20
12
17
Kvænangen
Eide
04
Reisafjord
Uløya
UL248
08
12
20
32
02
Straum-
fjord
Rappesvarre
18
Sørkjosen
15
06
Lyngen
Vaddas
Nordmannvik
N
Kåfjord
06
25
Sample site
0
5
10 km
Poles to S2 foliation
Poles to S1 foliation in KNC
Poles to S1 foliation in RNC
L2 lineation
L1 lineation
Fold hinges (L2)
Poles to fold axial planes (S2)
Structures
Nappe Boundary
Fault
S2 foliation
L2 stretching lineation
Kalak Nappe Complex
Metasediments, ortho- and paragneiss, undifferentiated
Lyngsfjellet Nappe Complex
Reisa Nappe Complex
Granite
Gabbro
Nordmannvik Nappe
Kåfjord Nappe
Vaddas Nappe
A′
B′
Arnøya
Kågen
Eide
C′
D′
Lyngen
Nordmannvik
Sørkjosen

Fig. 2

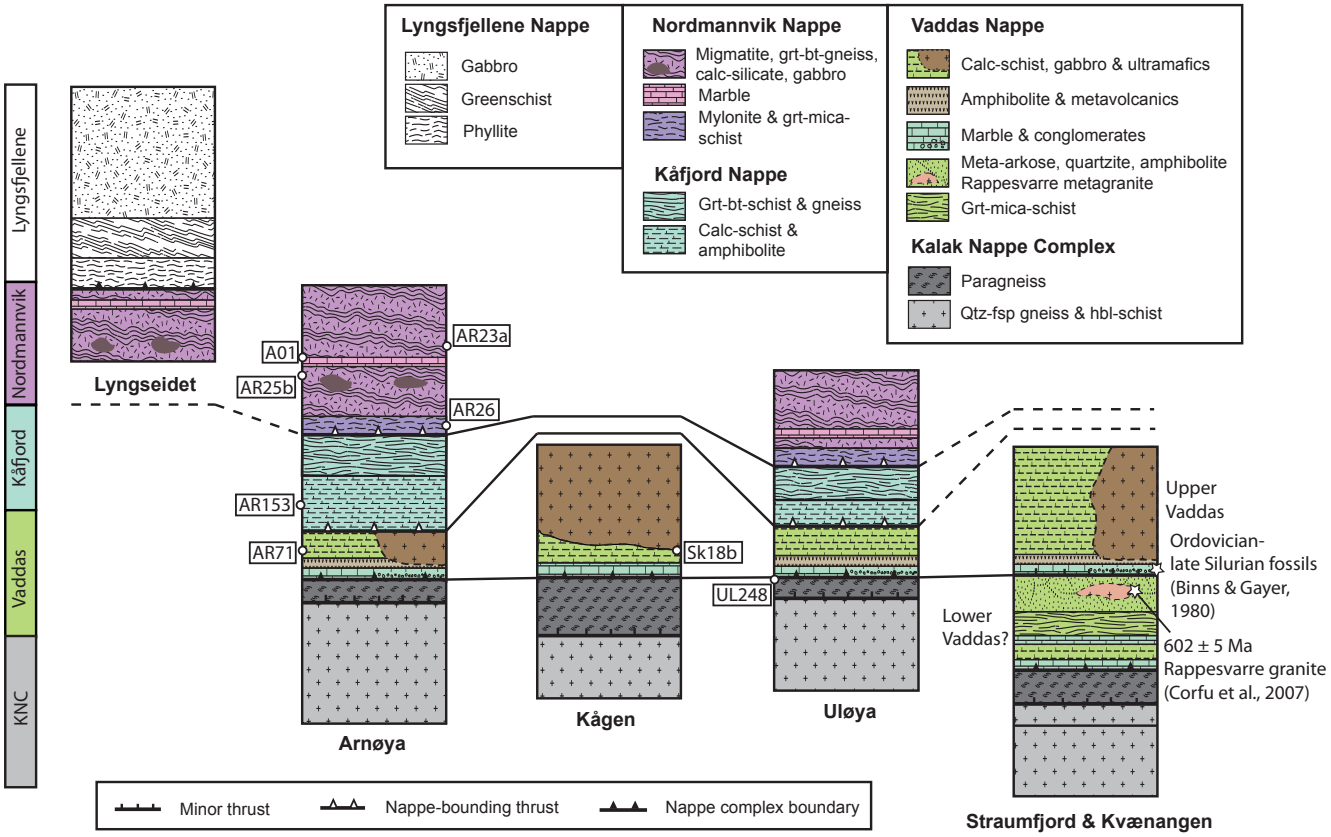
Lyngsfjellene Nappe
Gabbro
Greenschist
Phyllite
Nordmannvik Nappe
Migmatite, grt-bt-gneiss, calc-silicate, gabbro
Marble
Mylonite & grt-mica-schist
Kåfjord Nappe
Grt-bt-schist & gneiss
Calc-schist & amphibolite
Vaddas Nappe
Calc-schist, gabbro & ultramafics
Amphibolite & metavolcanics
Marble & conglomerates
Meta-arkose, quartzite, amphibolite
Rappesvarre metagranite
Grt-mica-schist
Kalak Nappe Complex
Paragneiss
Qtz-fsp gneiss & hbl-schist
Lyngsfjellene
Nordmannvik
Kåfjord
Vaddas
KNC
Lyngseidet
A01
AR25b
AR23a
AR26
AR153
AR71
Arnøya
Sk18b
Kågen
UL248
Uløya
Lower Vaddas?
Upper Vaddas
Ordovician-late Silurian fossils (Binns & Gayer, 1980)
602 ± 5 Ma Rappesvarre granite (Corfu et al., 2007)
Straumfjord & Kvænangen
Minor thrust
Nappe-bounding thrust
Nappe complex boundary

Fig. 3

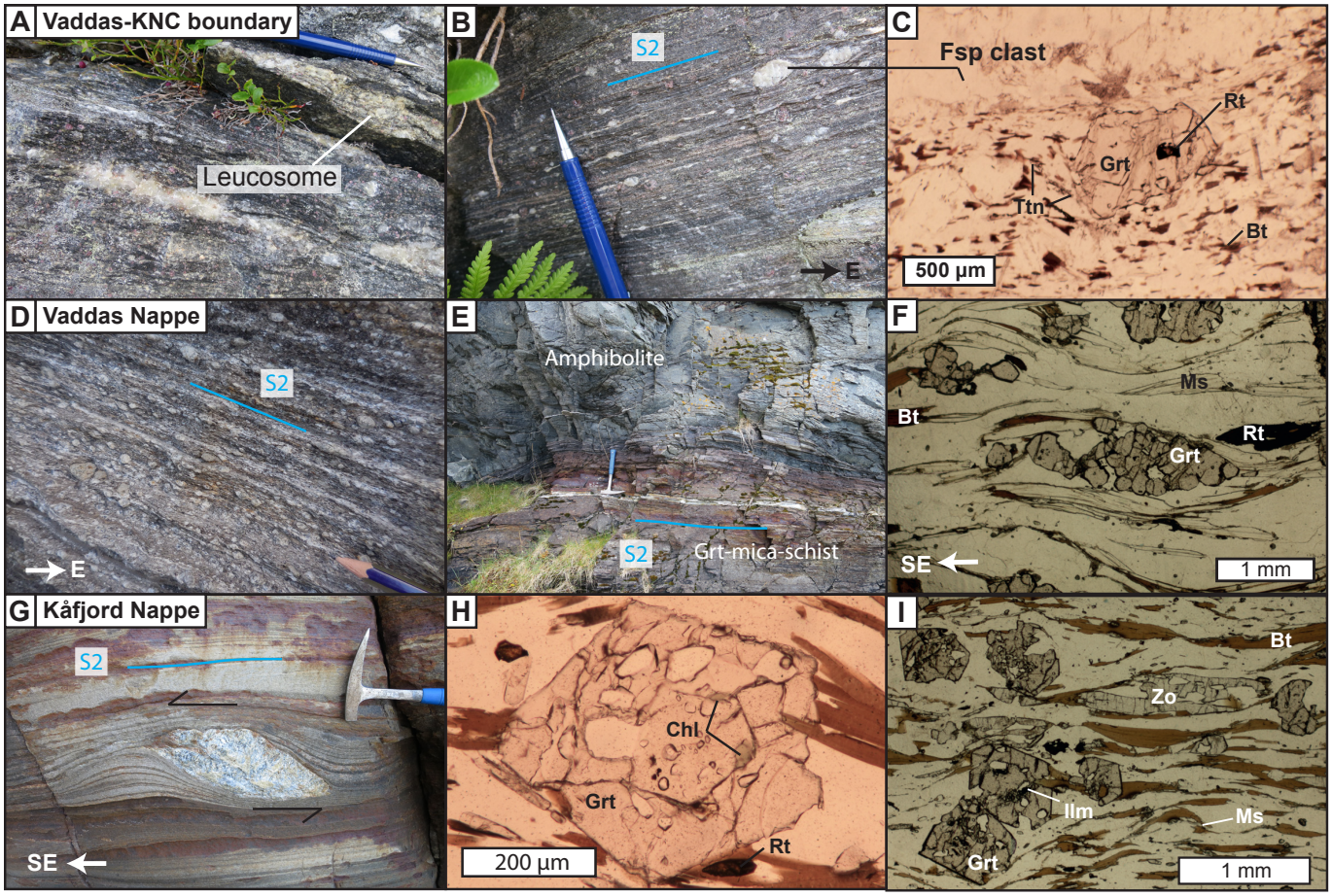
A
Vaddas-KNC boundary
Leucosome
B
S2
E
C
Fsp clast
Rt
Grt
Ttn
Bt
500 µm
D
Vaddas Nappe
S2
E
E
Amphibolite
S2
Grt-mica-schist
F
Ms
Bt
Rt
Grt
SE
1 mm
G
Kåfjord Nappe
S2
SE
H
Chl
Grt
Rt
200 µm
I
Bt
Zo
Ilm
Ms
Grt
1 mm

Fig. 4

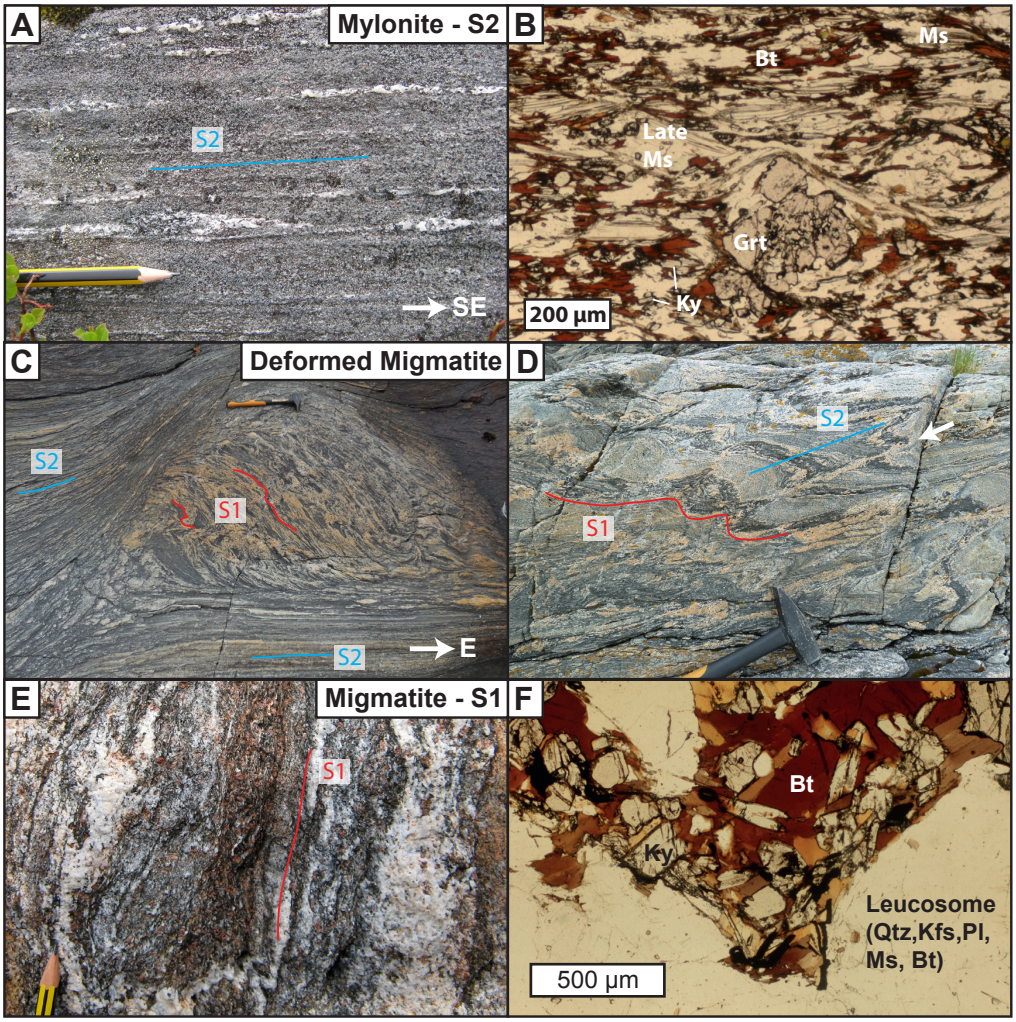
A
Mylonite - S2
S2
SE
B
Ms
Bt
Late
Ms
Grt
Ky
200 µm
C
Deformed Migmatite
S2
S1
S2
E
D
S2
S1
E
Migmatite - S1
S1
F
Bt
Ky
Leucosome
(Qtz,Kfs,Pl,
Ms, Bt)
500 µm

Fig. 5

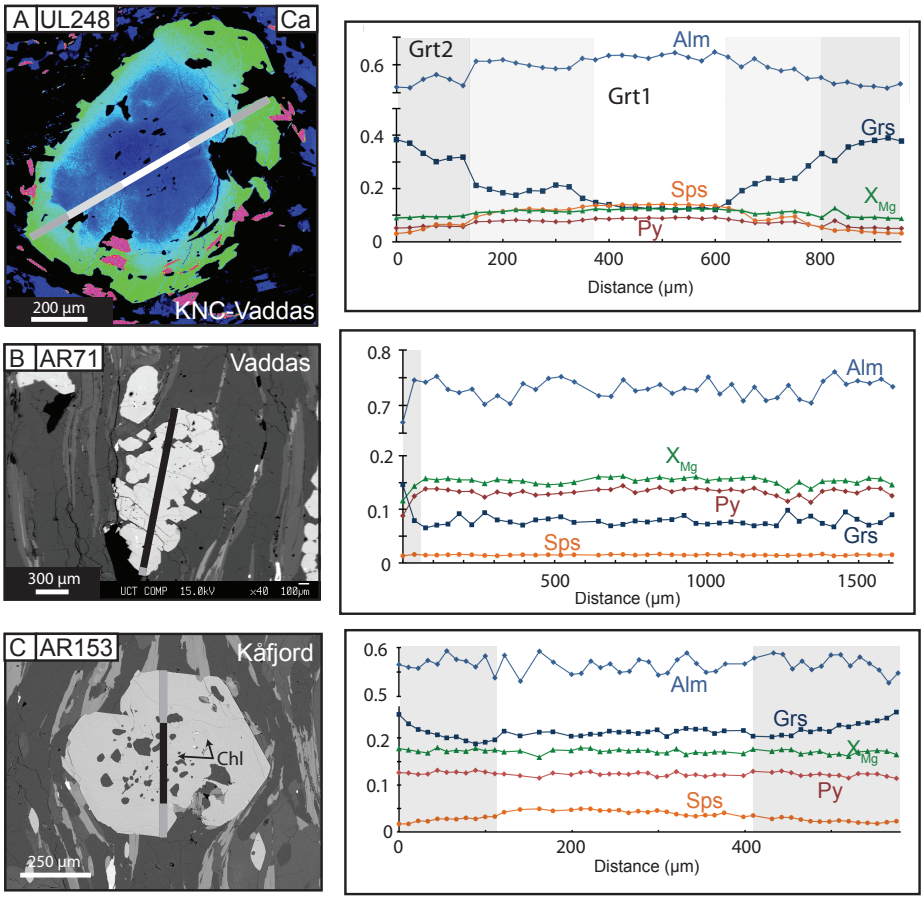
A UL248
Ca
200 µm
KNC-Vaddas
Grt2
Grt1
Alm
Grs
Sps
Py
X_{Mg}
Distance (µm)
B AR71
Vaddas
300 µm
Alm
X_{Mg}
Py
Grs
Sps
Distance (µm)
C AR153
Kåfjord
Chl
250 µm
Alm
Grs
X_{Mg}
Py
Sps
Distance (µm)

Fig. 6

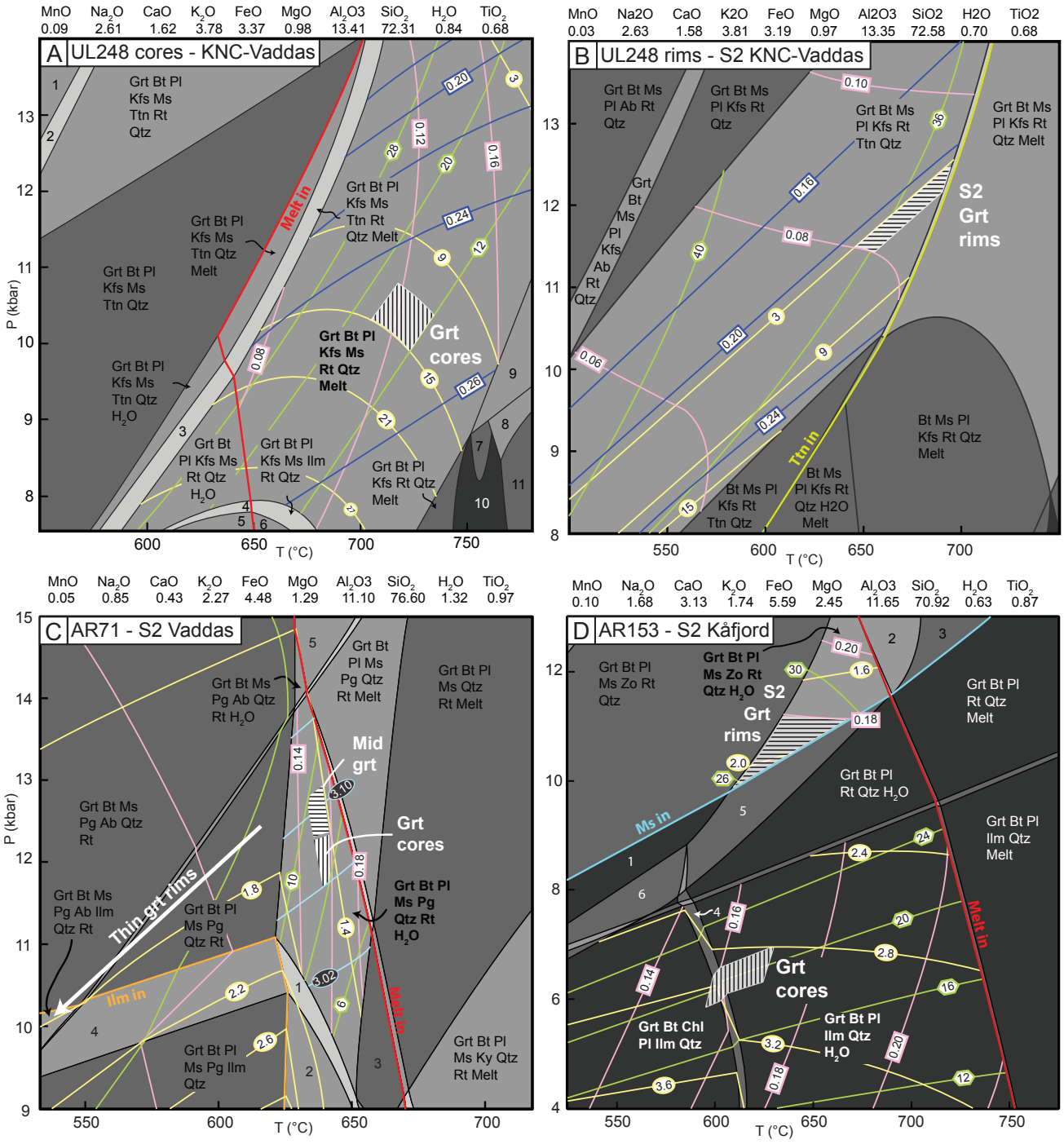

Fig. A
1. Grt-Bt-Pl-Ms-Ttn-Rt-Ab-Qtz
2. Grt-Bt-Pl-Kfs-Ms-Ttn-Ab-Rt-Qtz
3. Grt-Bt-Pl-Kfs-Ms-Ttn-Rt-Qtz-H_2O
4. Bt-Pl-Kfs-Ms-Ilm-Rt-Qtz-H_2O
5. Bt-Pl-Kfs-Ms-Ilm-Rt-Qtz-H_2O
6. Bt-Pl-Kfs-Ms-Ilm-Rt-Qtz-Melt
7. Grt-Bt-Pl-Kfs-Sil-Qtz-Melt
8. Grt-Bt-Pl-Kfs-Sil-Rt-Qtz-Melt
9. Grt-Bt-Pl-Kfs-Ky-Rt-Qtz-Melt
10. Grt-Bt-Pl-Kfs-Qtz-Melt
11. Grt-Bt-Pl-Kfs-Ilm-Qtz-Melt

Fig. C
1. Grt Bt Pl Ms Pg Im Qtz Rt H_2O
2. Grt Bt Pl Ms Pg Ilm Qtz H_2O
3. Grt Bt Pl Ms Qtz Rt H_2O
4. Grt Bt Pl Ms Pg Ilm Qtz Rt
5. Grt Bt Ms Pg Ab Qtz Rt

Fig. D
1. Grt-Bt-Pl-Zo-Rt-Qtz
2. Grt-Bt-Pl-Ms-Zo-Rt-Qtz-Melt
3. Grt-Bt-Pl-Ms-Rt-Qtz-Melt
4. Grt-Bt-Chl-Pl-Qtz-H_2O
5. Grt-Bt-Pl-Zo-Rt-Qtz-H_2O
6. Grt-Bt-Pl-Chl-Zo-Rt

Fig. 7

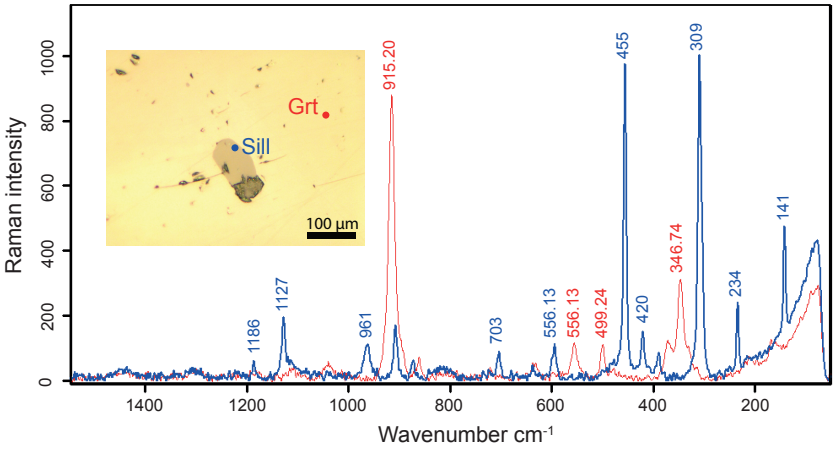
Raman intensity
0
200
400
600
800
1000
1400
1200
1000
800
600
400
200
Wavenumber cm-1
Grt
Sill
100 µm
1186
1127
961
915.20
703
556.13
556.13
499.24
455
420
346.74
309
234
141

Fig. 8

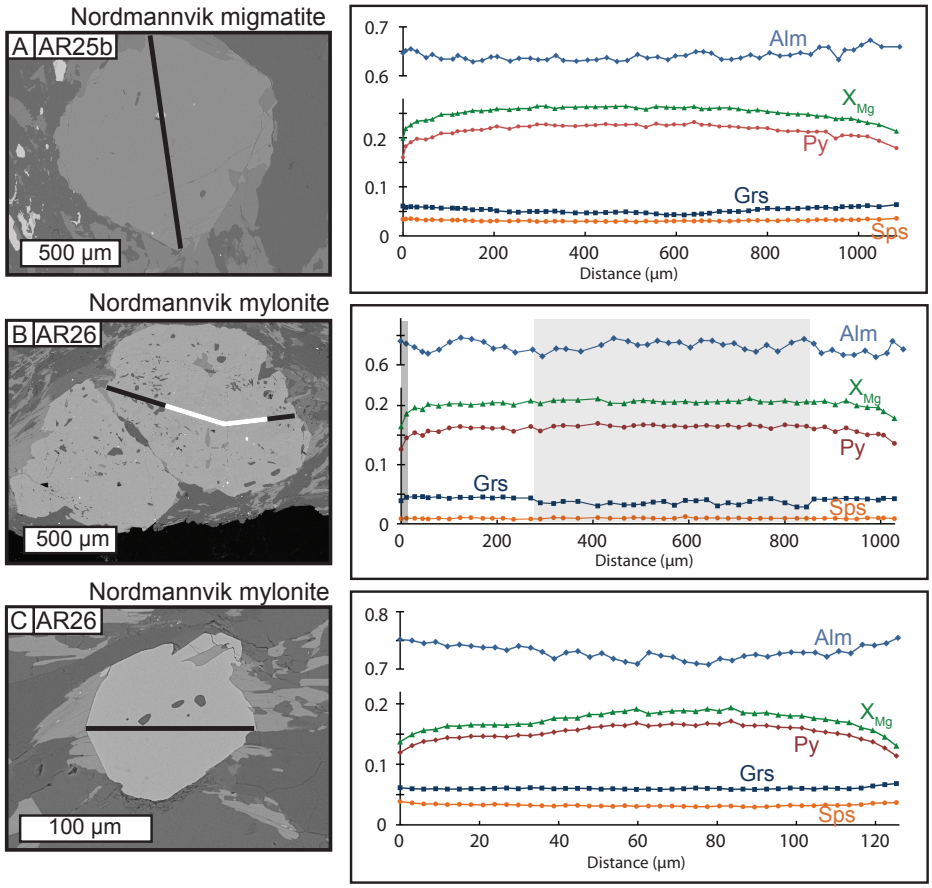
Nordmannvik migmatite
A AR25b
500 µm
Alm
X Mg
Py
Grs
Sps
Distance (µm)
Nordmannvik mylonite
B AR26
500 µm
Alm
X Mg
Py
Grs
Sps
Distance (µm)
Nordmannvik mylonite
C AR26
100 µm
Alm
X Mg
Py
Grs
Sps
Distance (µm)

Fig. 9

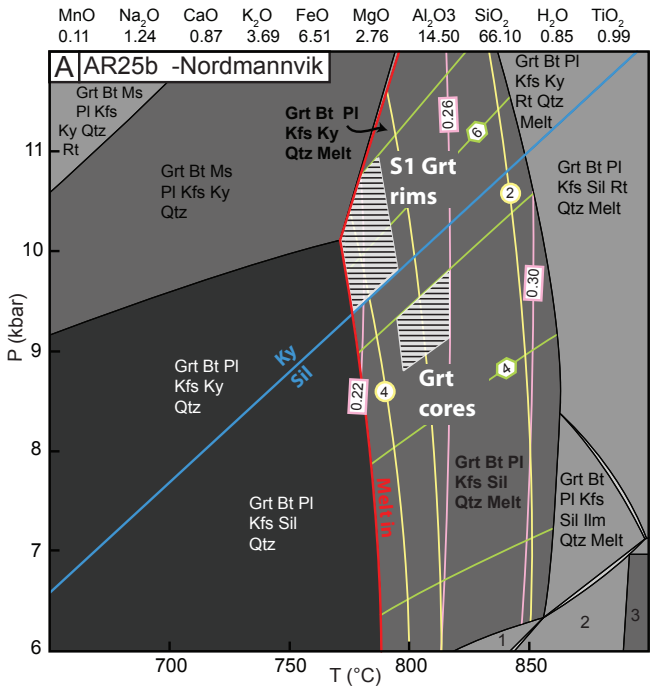

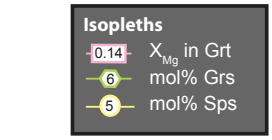

Fig. A

1. Grt Bt Crd Kfs Pl Sil Qtz Melt
2. Grt Bt Pl Kfs Crd Ilm Qtz Melt
3. Grt Crd Kfs Pl Ilm Qtz Melt

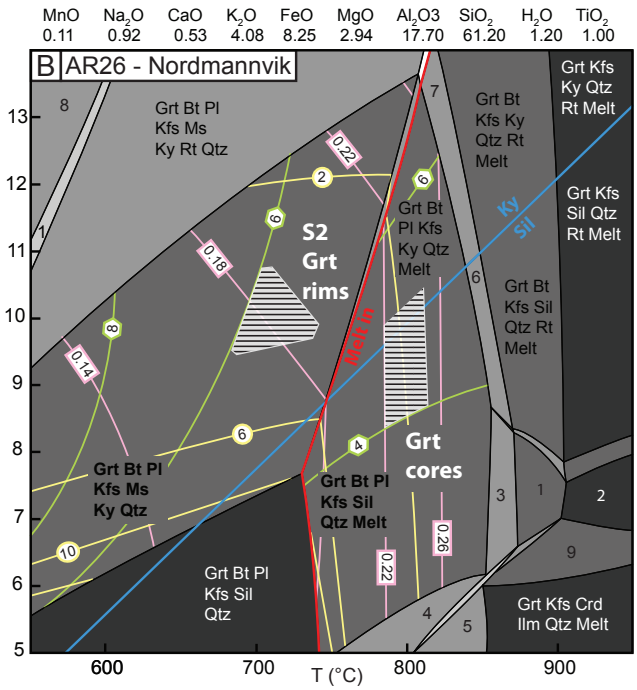

Fig. B

1. Grt Bt Kfs Sil Ilm Qtz Melt
2. Grt Kfs Sil Ilm Qtz Melt
3. Grt Bt Pl Kfs Sil Ilm Qtz Melt
4. Grt Bt Pl Kfs Crd Sil Qtz Melt
5. Grt Bt Crd Pl Kfs Ilm Qtz Melt
6. Grt Bt Pl Kfs Sil Qtz Rt Melt
7. Grt Bt Pl Kfs Ky Qtz Rt Melt
8. Grt Bt Pl Ab Ms Ky Qtz Rt
9. Grt Kfs Crd Sil Ilm Qtz Melt

Fig. 10

Zircon from Nordmannvik Restite (AR23a)

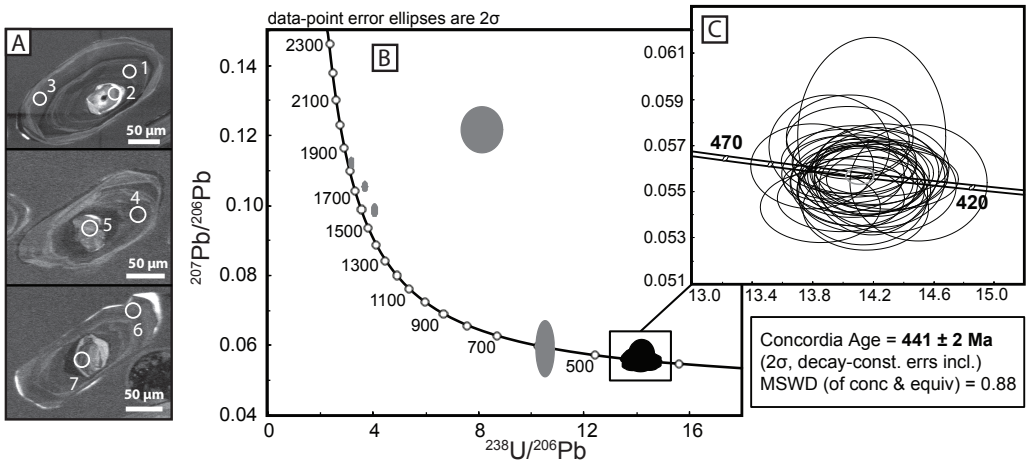

Zircon from Nordmannvik Leucosome (AR23a)

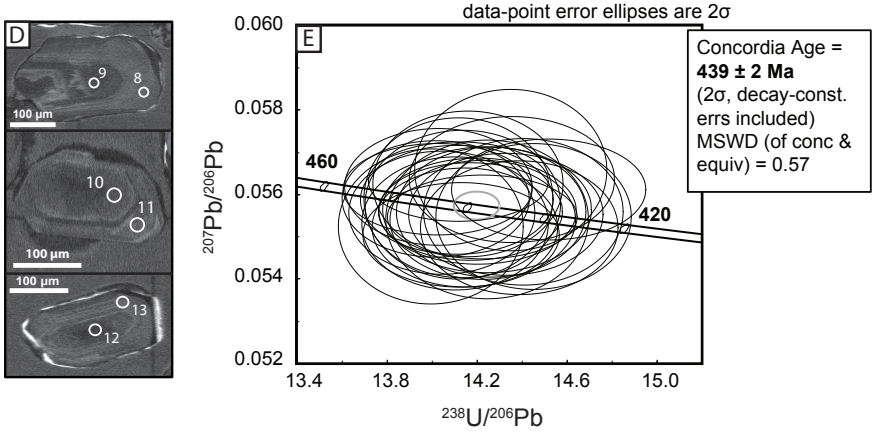

Titanite from Nordmannvik Nappe Calc-silicate lens (A01)

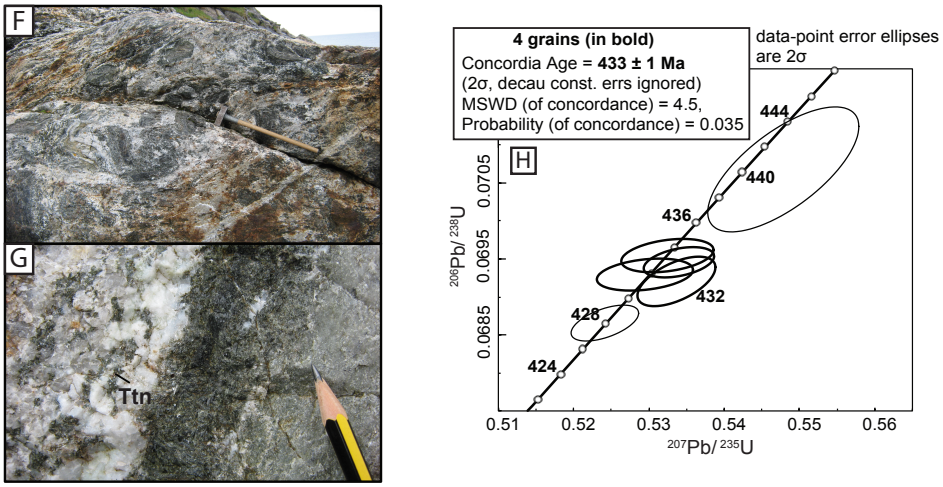

Fig. 11

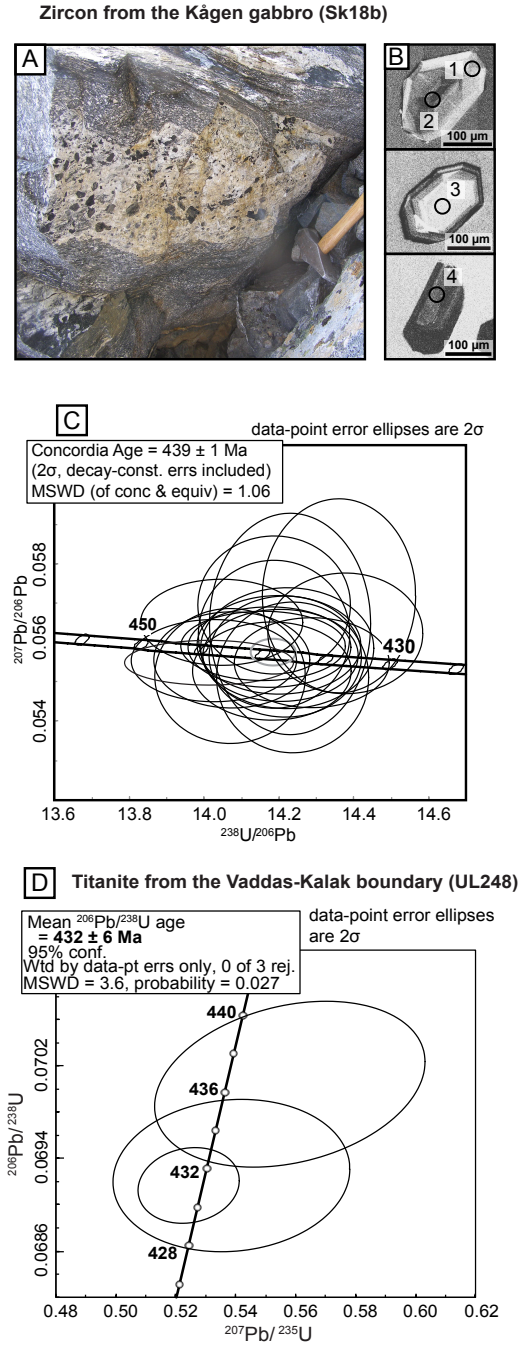
Zircon from the Kågen gabbro (Sk18b)
A
B
1
2
100 µm
3
100 µm
4
100 µm
C
data-point error ellipses are 2σ
Concordia Age = 439 ± 1 Ma
(2σ, decay-const. errs included)
MSWD (of conc & equiv) = 1.06
450
430
207Pb/206Pb
0.058
0.056
0.054
13.6
13.8
14.0
14.2
14.4
14.6
238U/206Pb
D
Titanite from the Vaddas-Kalak boundary (UL248)
Mean 206Pb/238U age
= 432 ± 6 Ma
95% conf.
Wtd by data-pt errs only, 0 of 3 rej.
MSWD = 3.6, probability = 0.027
data-point error ellipses
are 2σ
440
436
432
428
206Pb/238U
0.0702
0.0694
0.0686
0.48
0.50
0.52
0.54
0.56
0.58
0.60
0.62
207Pb/235U

Fig. 12

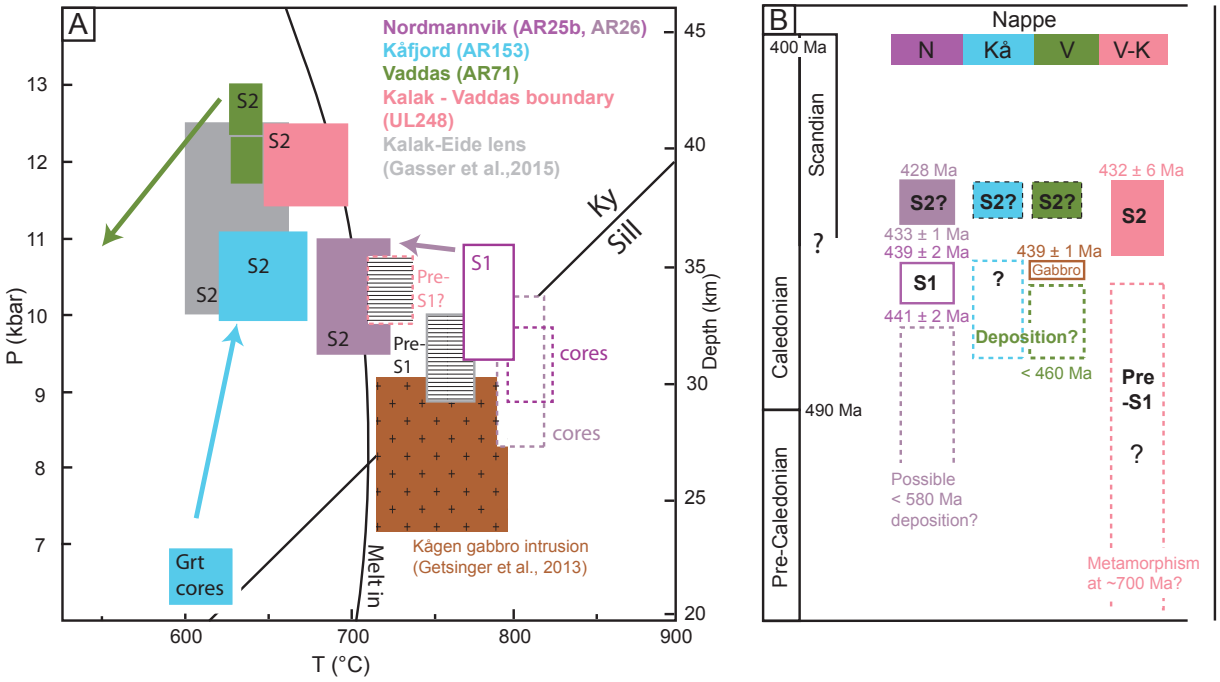
A
Nordmannvik (AR25b, AR26)
Kåfjord (AR153)
Vaddas (AR71)
Kalak - Vaddas boundary (UL248)
Kalak-Eide lens (Gasser et al.,2015)
S2
S2
S2
S2
S2
S1
Pre-S1?
Pre-S1
cores
cores
Ky
Sill
Grt cores
Melt in
Kågen gabbro intrusion (Getsinger et al., 2013)
P (kbar)
T (°C)
Depth (km)
B
Nappe
N
Kå
V
V-K
400 Ma
Scandian
Caledonian
490 Ma
Pre-Caledonian
428 Ma
S2?
S2?
S2?
432 ± 6 Ma
S2
433 ± 1 Ma
439 ± 2 Ma
S1
?
439 ± 1 Ma
Gabbro
441 ± 2 Ma
Deposition?
< 460 Ma
Pre -S1
?
Possible < 580 Ma deposition?
Metamorphism at ~700 Ma?

Fig. 13

A. Relative relationships between units along the pre-Scandian Baltica edge

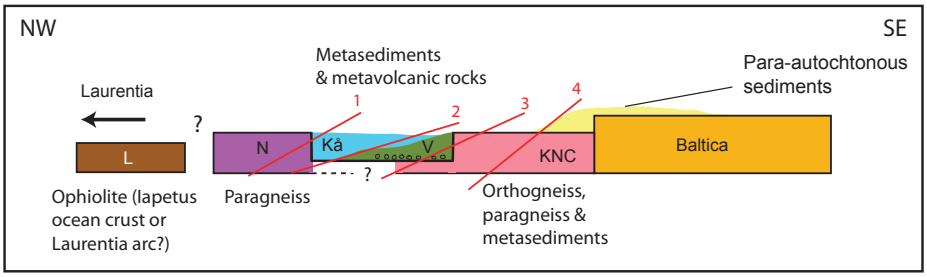

B. Schematic overview of Caledonian subduction and nappe-stacking

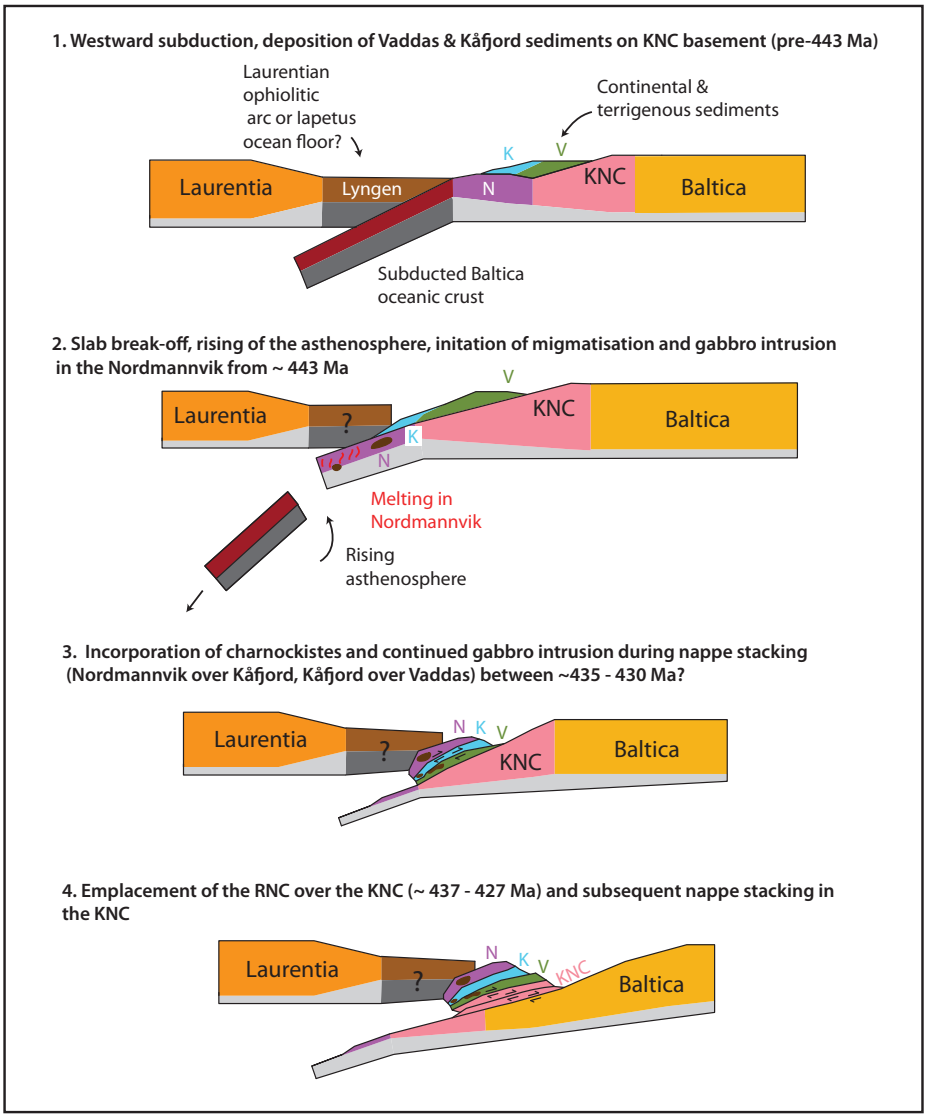

Fig. 14

Table 1: List of samples showing location, context and methods

Sample	Nappe	Rock type	Sample site	Method	Context
UL248	Kalak-Vaddas	Grt-bt-mylonite	N69.86755 °, E20.60304°	P-T modelling, U-Pb titanite	Lower part of ~40 m-thick mylonite zone
AR71	Vaddas	Grt-micaschist	N70.06315°, E20.45522°	P-T modelling	Upper ~30 m of ~120m-thick Vaddas Nappe
Sk18b	Vaddas	Gabbroic pegmatite	N69.985900°, E20.829567°	U-Pb zircon	Pegmatite near the edge of Kågen gabbro
AR153	Kåfjord	Grt-bt-zo-schist	N70.06797 °, E20.44341°	P-T modelling	Mid- to lower- Kåfjord Nappe
AR23a	Nordmannvik	Pelitic migmatite	N70.205343°, E20.522562°	U-Pb zircon	Lens with S1 foliation
AR25b	Nordmannvik	Pelitic migmatite	N70.16425°, E20.52112°	P-T modelling	Lens with S1 foliation
AR26	Nordmannvik	Grt-bt-ky-schist	N70.137455°, E20.561118°	P-T modelling	Mylonite ~50 m above Nordmannvik-Kåfjord boundary (S2 foliation)
A01	Nordmannvik	Calc-silicate	N70.191422°, E20.503611°	U-Pb titanite	S1 lens, interaction zone between calc-silicate layers and leucosome

Table 2: Mineralogy of petrology samples

		Main minerals										Accessory minerals						
Nappe	Sample	Bt	Pl	Qtz	Grt	Kfs	Sil	Ky	Zo	Ms	Chl	Zrn	Mnz	Rt	Ttn	Ill	Ap	Ep/All
Kalak-Vaddas	UL248	x	x	x	x	x				x		x		x	x	x	x	x
Vaddas	AR71	x	x	x	x					x		x		x		x	x	
Kåfjord	AR153	x	x	x	x				x	x	Gt in.	x		x	x	x	x	
Nordmannvik	AR25b	x	x	x	x	x	x	x		x		x	x			x	x	
Nordmannvik	AR26	x	x	x	x		Gt in.	x		x		x				x	x	

Table 3: Representative garnet compositions

Mineral	**Grt**																			
Nappe	Kalak-Vaddas Boundary				Vaddas				Kåfjord				Nordmannvik (migmatite)				Nordmannvik (mylonite)			
Sample	UL248				AR71				AR153				AR25b				AR26			
	Core (Grt1)	Rim (Grt2)	Core (Grt1)	Rim (Grt2)	Core	Rim (late)	Core	Rim	Core	Rim	Core	Rim	Core	Rim	Core	Rim	Grt core (lrg)	Grt rim (lrg)	Grt core (sml)	Grt rim (sml)
Wt%							*	*					*	*	*	*	*	*	*	*
SiO_2	37.63	38.01	37.47	38.00	37.74	37.76	37.72	37.58	37.81	37.60	37.60	37.59	38.61	38.14	37.87	37.59	37.76	37.67	37.72	37.91
TiO_2	0.00	0.07	0.00	0.08	0.07	0.04	0.00	0.00	0.13	0.05	0.01	0.05	0.03	0.04	0.00	0.00	0.01	0.03	0.01	0.03
Al_2O_3	21.64	21.41	21.49	21.46	21.81	21.82	22.00	21.77	21.94	22.51	22.05	22.57	22.00	21.92	21.89	21.64	21.67	21.60	21.76	21.56
Fe_2O_3	0.00	0.63	0.00	0.00	0.00	0.00	0.00	0.00	0.00	0.00	0.00	0.00	0.00	0.00	0.00	0.00	0.00	0.00	0.00	0.00
FeO	28.74	24.13	29.33	24.01	33.44	31.45	32.71	33.26	27.08	26.12	28.03	27.25	30.13	31.28	31.35	31.21	33.77	34.26	32.25	33.00
MnO	6.25	1.66	6.06	1.76	0.69	0.63	0.64	0.70	1.54	0.80	1.55	0.86	1.44	1.61	1.62	1.63	0.49	0.52	1.53	1.58
MgO	2.24	1.38	2.28	1.32	3.48	2.32	3.54	3.18	3.06	3.25	3.13	3.09	5.90	4.63	5.32	4.85	4.53	4.08	4.54	3.53
CaO	4.52	13.46	4.02	13.38	2.73	5.35	2.62	3.19	7.91	8.79	6.89	8.04	1.70	2.07	2.06	2.50	1.56	1.68	2.11	2.18
Total	101.02	100.75	100.65	100.01	99.96	99.37	99.23	99.68	99.47	99.12	99.26	99.45	99.81	99.69	100.11	99.42	99.79	99.84	99.92	99.79
Si	2.991	2.986	2.993	3.003	3.011	3.034	3.029	3.008	3.001	2.978	2.995	2.972	3.030	3.032	2.988	2.993	3.009	3.010	2.998	3.013
Ti	0.000	0.004	0.000	0.004	0.004	0.002	0.000	0.000	0.008	0.003	0.001	0.003	0.002	0.002	0.000	0.000	0.001	0.002	0.001	0.002
Al	2.028	1.983	2.023	1.999	2.051	2.067	2.082	2.054	2.053	2.101	2.070	2.103	2.042	2.054	2.036	2.031	2.036	2.034	2.038	2.023
Fe^{3+}	0.000	0.037	0.000	0.000	0.000	0.000	0.000	0.000	0.000	0.000	0.000	0.000	0.000	0.000	0.000	0.000	0.000	0.000	0.000	0.000
Fe^{2+}	1.910	1.585	1.959	1.587	2.231	2.113	2.196	2.226	1.797	1.730	1.867	1.801	1.984	2.079	2.068	2.078	2.250	2.289	2.143	2.205
Mn	0.421	0.110	0.410	0.118	0.046	0.043	0.044	0.047	0.104	0.054	0.105	0.058	0.096	0.108	0.108	0.110	0.033	0.035	0.103	0.100
Mg	0.265	0.161	0.271	0.155	0.414	0.278	0.424	0.379	0.362	0.384	0.372	0.364	0.692	0.549	0.626	0.576	0.538	0.486	0.538	0.468
Ca	0.385	1.133	0.344	1.133	0.233	0.461	0.225	0.274	0.673	0.746	0.588	0.681	0.143	0.176	0.174	0.213	0.133	0.144	0.180	0.188
X_{alm}	0.641	0.530	0.656	0.530	0.763	0.730	0.703	0.734	0.592	0.575	0.622	0.599	0.623	0.661	0.689	0.693	0.740	0.751	0.714	0.698
X_{prp}	0.089	0.054	0.091	0.052	0.142	0.096	0.136	0.125	0.119	0.127	0.124	0.121	0.217	0.174	0.209	0.192	0.177	0.159	0.179	0.153
X_{sps}	0.141	0.037	0.137	0.039	0.016	0.015	0.014	0.016	0.034	0.018	0.035	0.019	0.030	0.034	0.036	0.037	0.011	0.012	0.034	0.033
X_{grs}	0.129	0.379	0.115	0.379	0.080	0.159	0.072	0.090	0.221	0.248	0.196	0.226	0.045	0.056	0.058	0.071	0.044	0.047	0.060	0.061
X_{Mg}	0.122	0.092	0.122	0.089	0.156	0.116	0.162	0.146	0.168	0.182	0.166	0.168	0.259	0.209	0.232	0.217	0.193	0.175	0.201	0.175

* EDS SEM analyses

Table 4: Representative compositions of muscovite, biotite and plagioclase

Mineral	Muscovite						Biotite									Plagioclase						
Sample	UL248		AR71	AR153	AR26	AR25b	UL248		AR71	AR153		AR26		AR25b		UL248		AR71	AR153	AR26	AR25b	
	Early	Late				Late	Grt in.	Mtx		Early	Late	Grt in.	Mtx	Restite	Leuco	Core	Rim				Restite	Leuco
Wt%																						
SiO_2	46.32	48.26	46.69	48.33	45.72	45.31	36.79	36.29	36.98	38.06	38.26	37.82	36.18	36.04	36.05	61.17	62.75	64.92	60.48	63.01	61.51	61.79
TiO_2	1.08	1.00	0.84	0.94	1.27	1.79	3.53	2.95	2.33	1.93	0.78	3.58	4.58	3.84	3.67	0.00	0.00	0.00	0.00	0.00	0.02	0.01
Cr_2O_3	0.03	0.03	0.02	0.02	0.04	0.05	0.01	0.01	0.05	0.10	0.03	0.00	0.00	0.11	0.02	0.00	0.00	0.00	0.00	0.00	0.00	0.00
Al_2O_3	33.27	30.78	34.06	32.99	34.67	34.24	17.33	16.94	18.57	20.60	19.53	20.57	17.69	18.74	19.36	23.95	23.01	23.27	25.40	23.34	24.60	24.95
Fe_2O_3	2.15	0.84	0.00	0.00	0.00	1.26	0.00	0.00	0.00	0.00	0.00	0.00	0.00	0.00	0.00	0.04	0.20	0.00	0.01	0.00	0.00	0.00
FeO	0.47	1.83	1.40	1.63	1.06	0.27	21.55	21.26	19.44	15.98	16.50	13.80	18.48	17.95	17.52	0.00	0.00	0.00	0.00	0.06	0.00	0.04
MnO	0.02	0.05	0.02	0.00	0.00	0.00	0.23	0.22	0.05	0.05	0.04	0.01	0.00	0.04	0.06	0.00	0.00	0.00	0.05	0.03	0.06	0.03
MgO	1.09	1.76	1.44	1.61	1.07	1.16	6.82	7.81	11.46	11.69	13.59	11.62	9.13	11.45	10.33	0.00	0.00	0.01	0.00	0.00	0.00	0.00
CaO	0.00	0.00	0.00	0.00	0.00	0.00	0.02	0.00	0.00	0.00	0.01	0.09	0.00	0.00	0.00	5.48	4.44	3.69	5.59	4.95	5.85	6.16
Na_2O	0.36	0.25	1.11	0.76	0.40	0.34	0.10	0.07	0.22	0.19	0.17	0.00	0.09	0.16	0.11	8.58	9.34	9.18	8.34	8.61	8.16	7.93
K_2O	11.25	11.30	9.46	10.17	10.55	11.14	10.03	10.16	8.17	8.94	9.03	9.09	8.89	10.03	10.18	0.22	0.22	0.05	0.07	0.18	0.28	0.23
Total	96.03	96.10	95.04	96.46	94.77	95.57	96.41	95.70	97.27	97.54	97.93	96.58	95.04	98.36	97.29	99.43	99.96	101.12	99.94	100.18	100.48	101.14
Si	3.086	3.216	3.112	3.187	3.069	3.026	2.906	2.870	2.820	2.860	2.839	2.873	2.864	2.712	2.749	2.726	2.772	2.843	2.683	2.792	2.721	2.721
Ti	0.054	0.050	0.042	0.047	0.064	0.090	0.210	0.175	0.134	0.109	0.044	0.204	0.273	0.217	0.210	0.000	0.000	0.000	0.000	0.000	0.001	0.000
Cr	0.001	0.001	0.001	0.001	0.002	0.003	0.001	0.000	0.003	0.006	0.002	0.000	0.000	0.006	0.001	0.000	0.000	0.000	0.000	0.000	0.000	0.000
Al	2.613	2.418	2.676	2.564	2.743	2.695	1.614	1.579	1.669	1.824	1.708	1.842	1.651	1.662	1.740	1.258	1.198	1.201	1.328	1.219	1.283	1.295
Fe^{3+}	0.108	0.042	0.000	0.000	0.000	0.063	0.000	0.000	0.000	0.000	0.000	0.000	0.000	0.000	0.000	0.001	0.007	0.000	0.000	0.000	0.000	0.000
Fe^{2+}	0.026	0.102	0.078	0.090	0.059	0.015	1.424	1.406	1.240	1.004	1.024	0.877	1.223	1.129	1.117	0.000	0.000	0.000	0.000	0.002	0.000	0.001
Mn	0.001	0.003	0.001	0.000	0.000	0.000	0.015	0.015	0.003	0.003	0.003	0.001	0.000	0.003	0.004	0.000	0.000	0.000	0.002	0.001	0.002	0.001
Mg	0.108	0.175	0.143	0.159	0.107	0.115	0.803	0.920	1.303	1.309	1.503	1.316	1.077	1.284	1.174	0.000	0.000	0.000	0.000	0.000	0.000	0.000
Ca	0.000	0.000	0.000	0.000	0.000	0.000	0.002	0.000	0.000	0.000	0.001	0.007	0.000	0.000	0.000	0.262	0.210	0.173	0.266	0.235	0.277	0.291
Na	0.046	0.033	0.143	0.097	0.052	0.044	0.015	0.010	0.033	0.028	0.024	0.000	0.014	0.023	0.016	0.741	0.800	0.779	0.717	0.740	0.700	0.677
K	0.956	0.961	0.804	0.855	0.903	0.949	1.011	1.025	0.795	0.857	0.855	0.881	0.898	0.963	0.990	0.012	0.012	0.003	0.004	0.010	0.016	0.013
X_{Mg}							0.361	0.396	0.512	0.566	0.595	0.600	0.468	0.532	0.512							
An %																26	21	18	27	24	28	30

Supplementary information for:

PAPER II

Dismembering of subducted continental crust by nappe-stacking during Scandian continental collision: an example from the Reisa Nappe Complex, northern Norway

Faber, C., Stünitz, H., Gasser, D., Jeřábek, P., Kraus, K., Corfu, F., Ravna, E.K., and Konopásek, J.

Analytical methods

Table S1: XRF bulk composition analyses for petrology samples

Table S2: SIMS U-Th-Pb zircon data for migmatite sample AR23a leucosome and restite, and pegmatitic gabbro sample SK18b

Table S3: U-Pb TIMS data for titanite

SUPPORTING INFORMATION FOR:

Dismembering of subducted continental crust by nappe-stacking during Scandian continental collision: an example from the Reisa Nappe Complex, northern Norway

Carly Faber[1], Holger Stünitz[1], Deta Gasser[2,3], Petr Jeřábek[4], Katrin Kraus[1], Fernando Corfu[5], Erling Krogh Ravna[1]; Jiří Konopásek[1]

[1]Department of Geosciences, UiT The Arctic University of Norway, Tromsø, N-9037, Norway
[2]Western Norway University of Applied Sciences, Sogndal 6851, Norway
[3]Geological Survey of Norway, Trondheim 7491, Norway
[4]IPSG, Faculty of Science, Charles University, Albertov 6, 128 43, Prague 2, Czech Republic
[5]Department of Geosciences & Centre for Earth Evolution and Dynamics, University of Oslo, Norway

Appendix S1 – Analytical methods

Bulk rock X-ray fluorescence analyses were performed with a Panalytical Axios XRF spectrometer at the University of Cape Town, South Africa. Analyses for eleven major elements (Fe, Mn, Ti, Ca, K, S, P, Si, Al, Mg, and Na) were performed on fused disks prepared with a lithium borate flux. Loss on ignition (LOI) was determined from weight loss of the samples after 1.5 h ignition at 1050 °C (Table S1). Compositions of garnet (Table S2), biotite, feldspar, and white mica (Table S3) were measured using three instruments. The above minerals in samples AR25b, AR26, AR71 and AR153 were measured using a JEOL JXA-8100 electron microprobe at the University of Cape Town. Analyses were carried out using a 15 kV accelerating voltage, 20 nA probe current and 2-3 μm spot size. Counting times were 5 seconds for both background and 10 seconds for peaks on all elements. Data were processed using ZAF matrix corrections and reduced with the PAP procedure.

The composition of minerals in sample UL248 were analyzed using a JEOL JXA-8900R electron microprobe at the Christian-Albrechts University in Kiel, Germany. Analyses were carried out using an accelerating voltage of 15 kV and beam current

of 15 nA. Counting times for background was 7 seconds and for peaks was 15 seconds. Garnet, biotite and muscovite were measured with a fully focused beam of 1 μm diameter and feldspar was measured with a 5 μm beam. Matrix corrections were carried out according to the CITZAF procedure version 3.5 in the JEOL software. The garnet map for sample UL248 was produced by dividing the mapped area into a grid of measuring points on which counting rates were generated to obtain relative element concentrations. Garnet compositions in samples AR25b and AR26 were determined on a Zeiss Merlin VP SEM housed at the University of Tromsø by semi-quantitative Energy Dispersive Spectroscopy (Oxford X-mag 80 detector) running Aztec 3.3 software. The EDS system is consistently calibrated using a cobalt standard. Consistency of the EDS analyses with microprobe analyses was checked by analyzing a common sample (AR71; table S2), and results do not differ.

Zircon and titanite were separated from crushed samples by standard mineral enrichment techniques and hand picked under a binocular microscope. Zircon was mounted in epoxy and polished to reveal grain cores. CL images of grains guided SIMS U-Th-Pb zircon geochronology . Analyses were carried out in two separate sessions on three zircon separates on the Cameca IMS 1270 large-geometry ion microprobe at the Nordsim facility at the Swedish Museum of Natural History (methodology of Whitehouse and Kamber, 2005 and references therein). An O_2^- primary beam with 23 kV incident energy (-13kV primary, +10 kV secondary) was used to sputter zircon, with the primary beam operated in aperture illumination (Köhler) mode yielding a ~15-20 μm spot which was presputtered using a 25 μm raster for 90 s to remove gold and minimise surface contamination. For zircon, centring of the secondary ion beam in the 4000 μm field aperture (FA), mass calibration optimisation, and optimisation of the secondary beam energy distribution in the 45eV energy window were performed automatically for each run using the $^{90}Zr_2{}^{16}O+$ species at nominal mass 196. Mass calibration of all peaks in the mono-collection sequence was performed at the start of each analytical session; while within run mass calibration optimisation scanned only $^{90}Zr_2{}^{16}O+$ to adjust the

mass calibration slope to account for small drift. A mass resolution (M/DM) of ~5400 was used to ensure adequate separation of Pb isotope peaks from nearby $HfSi^+$ species. Ion signals were detected using the axial ion-counting electron multiplier. All analyses were run in fully automated chain sequences. Zircon data reduction assumes a power law relationship between Pb^+/U^+ and UO_2^+/U^+ ratios with an empirically derived slope in order to calculate actual Pb/U ratios based on those in the 91500 reference zircon. The U concentration and Th/U ratio are also referenced to the Geostandards 91500 zircon, which has a $^{207}Pb/^{206}Pb$ age of 1065 Ma (Wiedenbeck *et al.*, 1995).

Titanites were analysed by U-Pb thermal ionoization mass spectrometry (TIMS) at the University of Oslo, Norway. Titanite grains were washed in dilute HNO_3, ionized water and acetone and an ultrasonic bath was used in order to remove any contamination. Each sample was weighed on a microbalance and spiked with a ^{202}Pb – ^{205}Pb – ^{235}U tracer. The samples were dissolved in HF and a drop of HNO_3 in Teflon bombs in an oven at ~195° overnight. The solutions were chemically separated using micro-columns and anion exchange resin to remove cations that may inhbit ionization (Krogh, 1973). The U-Pb solutions were dried down and loaded on degassed singe Re filaments with silica gel and measured on a Finnigan MAT 262 mass spectrometer. Details are given in Appendix A of Augland et al., (2010). The analytical error and corrections were incorporated and propagated using an in-house programe (ROMAGE 6.3). ISOPLOT 3.75 (Ludwig, 2012) was used for results from both zircon and titanite analyses.

References

Augland, L.E., Andresen, A. & Corfu, F., 2010, Age, structural setting, and exhumation of the Liverpool Land eclogite terrane, East Greenland Caledonides. *Lithosphere,* **2**, 267-286

Fuhrman, M.L. & Lindsley, H., 1988, Ternary-feldspar modeling and thermometry, *American Mineralogist*, **73**,201–215

Krogh, T.E., 1973, A low-contamination method for hydrothermal decomposition of zircon and extraction of U and Pb for isotopic age determination. *Geochimica et Cosmochimica Acta*, **37**, 485–494

Ludwig, K.R., 2001, Isoplot/Ex, rev. 2.49. A Geochronological Toolkit for Microsoft Excel: Berkeley Geochronology Center, Special Publication No. 1a

Tajčmanová, L., Connolly, J.A.D. & Cesare, B., 2009, A thermodynamic model for titanium and ferric iron solution in biotite. *Journal of Metamorphic Geology*, **27**, 153–165

Wiedenbeck, M., Allé, P., Corfu, F., Griffin, W.L., Meier, M., Oberli, F., von Quadt, A., Roddick, J. C. & Spiegel, W., 1995, Three natural zircon standards for U-Th-Pb, Lu-Hf, trace element and REE analysis. *Geostandards Newsletter*, **19**, 1- 23

Whitehouse, M.J. & Kamber, B., 2005, Assigning dates to thin gneissic veins in high-grade metamorphic terranes: a cautionary tale from Akilia, southwest Greenland. *Journal of Petrology*, **46**, 291-318

Table S1. XRF bulk composition analyses for petrology samples

Sample	UL248	AR71	AR153	AR25b	AR26
Na_2O	2.61	0.85	1.68	1.24	0.92
MgO	0.98	1.29	2.45	2.76	2.94
Al_2O_3	13.41	11.10	11.65	14.50	17.70
SiO_2	72.31	76.60	70.92	66.10	61.20
P_2O_5	0.10	0.08	0.15	0.14	0.20
K_2O	3.78	2.27	1.74	3.69	4.08
CaO	1.75	0.53	3.32	1.05	0.79
TiO_2	0.68	0.97	0.87	0.99	1.00
MnO	0.09	0.05	0.10	0.11	0.11
Fe_2O_3	3.74	4.98	6.21	7.23	9.17
Cr_2O_2	0.00	0.00	0.01	0.00	0.00
NiO	0.01	0.00	0.01	0.00	0.01
LOI	0.52	1.32	0.63	2.13	1.96
Total	99.98	100.04	99.75	99.94	100.08

Table S2. SIMS U-Th-Pb zircon data

								TW Concordia columns (Pbc corrected)				Ages					
Sample name	Sample/ spot #	[U] ppm	[Th] ppm	[Pb] ppm	Th/U calc	f_{206}%	$^{206}Pb/^{204}Pb$ measured	$^{238}U/^{206}Pb$	±σ %	$^{207}Pb/^{206}Pb$	±σ %	$^{207}Pb/^{206}Pb$	±σ	$^{207}Pb/^{235}U$	±σ	$^{206}Pb/^{238}U$	±σ
SK18b	n4287_@1	129.6	51.7	10.8	0.36	{0.11}	17723	14.1873	0.59	0.05695	1.26	490	27	447	5	439	2
SK18b	n4287_@02	257.7	168.5	23.1	0.67	{0.05}	36455	14.0740	0.61	0.05555	0.90	435	20	441	4	442	3
SK18b	n4287_@03	351.2	142.1	29.6	0.41	{0.02}	118706	14.0261	0.64	0.05554	0.77	434	17	442	4	444	3
SK18b	n4287_@04	327.1	229.1	29.8	0.67	{0.03}	55343	14.0470	0.63	0.05651	0.79	472	17	448	4	443	3
SK18b	n4287_@05	111.1	47.0	9.2	0.36	{0.08}	22932	14.3606	0.58	0.05718	1.76	499	38	444	7	434	2
SK18b	n4287_@06	180.8	74.0	15.2	0.44	{0.03}	64011	14.0695	0.58	0.05515	1.27	418	28	439	5	443	3
SK18b	n4287_@07	180.9	68.6	14.9	0.37	{0.03}	62516	14.2222	0.66	0.05585	1.12	447	25	439	5	438	3
SK18b	n4287_@08	164.5	64.4	13.7	0.40	{0.01}	235444	14.2170	0.59	0.05564	1.13	438	25	438	5	438	2
SK18b	n4287_@09	248.7	132.0	21.5	0.54	{0.04}	51198	14.2002	0.63	0.05594	0.91	450	20	440	4	439	3
SK18b	n4287_@10	399.9	185.3	33.8	0.45	0.04	49711	14.1747	0.63	0.05588	0.75	448	16	441	3	439	3
SK18b	n4287_@11	281.1	122.8	23.6	0.44	{0.03}	68872	14.2043	0.60	0.05567	0.86	439	19	439	4	439	3
SK18b	n4287_@12	167.6	69.4	13.9	0.40	{0.02}	92569	14.3776	0.59	0.05623	1.11	461	24	438	4	433	2
SK18b	n4287_@13	111.2	35.1	9.1	0.31	{0.03}	60238	14.1871	0.58	0.05621	1.36	461	30	443	5	439	2
SK18b	n4287_@14	291.3	119.2	24.1	0.41	{0.03}	61827	14.2878	0.59	0.05548	0.84	432	19	435	4	436	2
SK18b	n4287_@15	114.3	47.7	9.5	0.38	{0.08}	22977	14.2298	0.62	0.05647	2.03	471	44	443	8	438	3
SK18b	n4287_@16	157.1	61.7	13.0	0.42	{0.00}	>1e6	14.2366	0.58	0.05511	1.42	417	31	434	5	438	2
SK18b	n4287_@17	305.0	143.4	25.9	0.50	{0.00}	>1e6	14.1811	0.61	0.05527	0.92	423	20	437	4	439	3
SK18b	n4287_@19	1216.6	881.3	111.3	0.75	0.03	69939	14.0132	0.66	0.05548	0.42	432	9	442	3	444	3
SK18b	n4287_@20	489.1	178.1	40.4	0.36	{0.03}	54858	14.1578	0.64	0.05591	0.64	449	14	441	3	440	3
AR23a leuco	n5698@1	586.1	84.7	44.5	0.15	0.09	21390	14.5179	1.21	0.05612	0.87	457	19	434	5	429	5
AR23a leuco	n5698@12	297.3	31.0	22.7	0.11	{0.00}	>1e6	14.2625	1.21	0.05559	1.13	436	25	437	6	437	5
AR23a leuco	n5698@14	302.7	34.5	22.9	0.12	{0.03}	70554	14.4055	1.26	0.05559	1.28	436	28	433	6	433	5
AR23a leuco	n5698@16	684.4	81.0	53.4	0.12	{0.00}	>1e6	14.0242	1.22	0.05613	0.79	457	17	446	5	444	5
AR23a leuco	n5698@17	478.3	73.0	37.5	0.16	{0.00}	>1e6	14.1098	1.24	0.05588	0.94	448	21	442	6	441	5
AR23a leuco	n5698@17b	373.0	40.7	28.4	0.11	{0.00}	>1e6	14.3277	1.23	0.05553	1.06	434	24	435	6	435	5
AR23a leuco	n5698@18	304.2	34.2	23.5	0.12	{0.00}	>1e6	14.1365	1.25	0.05578	1.28	444	28	441	6	441	5
AR23a leuco	n5698@18b	618.5	118.5	48.7	0.20	{0.00}	418916	14.1705	1.18	0.05560	0.85	436	19	439	5	440	5
AR23a leuco	n5698@1b	446.0	67.3	34.7	0.16	{0.03}	71675	14.2024	1.26	0.05561	0.92	437	21	438	6	439	5
AR23a leuco	n5698@2	302.0	35.0	22.8	0.12	{0.02}	83456	14.4509	1.23	0.05548	1.27	432	28	431	6	431	5
AR23a leuco	n5698@20	385.2	49.0	29.7	0.13	{0.02}	76218	14.2251	1.18	0.05540	1.04	428	23	436	6	438	5
AR23a leuco	n5698@20b	475.8	74.9	37.5	0.16	{0.02}	84835	14.0159	1.21	0.05590	1.01	448	22	445	6	444	5
AR23a leuco	n5698@22	520.7	101.5	41.4	0.20	{0.02}	79027	14.0433	1.20	0.05557	1.07	435	24	442	6	443	5
AR23a leuco	n5698@23	1100.4	44.6	83.3	0.04	{0.01}	125138	14.1166	1.16	0.05631	0.68	465	15	445	5	441	5
AR23a leuco	n5698@24	317.1	48.5	24.4	0.16	{0.00}	>1e6	14.3494	1.22	0.05658	1.38	475	31	441	7	434	5
AR23a leuco	n5698@25	321.5	37.6	25.0	0.11	{0.00}	>1e6	13.9941	1.20	0.05525	1.36	422	30	441	7	445	5
AR23a leuco	n5698@26	439.2	71.7	34.4	0.16	{0.00}	>1e6	14.1022	1.20	0.05532	1.16	425	26	439	6	442	5
AR23a leuco	n5698@26b	573.9	108.2	45.2	0.19	{0.02}	79635	14.1457	1.19	0.05522	1.04	421	23	437	6	440	5
AR23a leuco	n5698@2b	298.5	19.3	22.3	0.07	{0.00}	>1e6	14.3872	1.25	0.05522	1.17	421	26	431	6	433	5
AR23a leuco	n5698@3	328.7	27.5	25.0	0.08	{0.02}	95618	14.2444	1.29	0.05541	1.39	429	31	436	7	437	5
AR23a leuco	n5698@32	353.0	30.7	27.0	0.09	{0.01}	147097	14.1592	1.22	0.05625	1.25	462	28	444	6	440	5
AR23a leuco	n5698@33	553.9	65.7	43.2	0.12	{0.00}	>1e6	14.0282	1.21	0.05618	1.01	460	22	446	6	444	5
AR23a leuco	n5698@35	295.8	33.5	22.9	0.11	{0.05}	40964	14.1169	1.21	0.05591	1.40	449	31	442	7	441	5
AR23a leuco	n5698@4	327.9	44.7	25.2	0.15	{0.00}	>1e6	14.3547	1.30	0.05636	1.08	466	24	439	6	434	5
AR23a leuco	n5698@4b	721.9	121.2	56.3	0.17	{0.00}	>1e6	14.2230	1.21	0.05547	0.73	431	16	437	5	438	5
AR23a leuco	n5698@5	463.2	82.1	36.4	0.18	{0.02}	96123	14.1288	1.26	0.05505	0.92	414	21	437	6	441	5
AR23a leuco	n5698@6	328.6	42.4	25.3	0.13	{0.05}	39685	14.2444	1.33	0.05564	1.10	438	24	437	6	437	6
AR23a rest	n5699@14	215.9	97.3	84.5	0.45	{0.00}	>1e6	3.1722	1.25	0.11225	0.57	1836	10	1799	12	1766	19
AR23a rest	n5699@2b	345.7	181.8	118.1	0.53	0.33	5592	3.6862	1.22	0.10540	0.57	1721	10	1622	11	1547	17
AR23a rest	n5699@23	215.3	79.0	64.1	0.37	{0.00}	>1e6	4.0556	1.21	0.09867	0.73	1599	14	1494	11	1421	15
AR23a rest	n5699@24b	590.8	168.6	88.9	0.36	0.15	12368	8.1285	3.96	0.12165	2.21	1981	39	1137	32	748	28
AR23a rest	n5699@1b	240.9	73.2	26.4	0.30	1.62	1155	10.5282	1.36	0.05905	5.55	569	121	582	26	585	8
AR23a rest	n5699@3	329.1	41.2	26.1	0.12	{0.00}	>1e6	13.7950	1.20	0.05610	1.34	456	30	452	7	451	5
AR23a rest	n5699@22	436.5	55.7	34.5	0.12	{0.01}	167827	13.8497	1.17	0.05433	1.15	385	26	439	6	449	5
AR23a rest	n5699@11	465.6	70.3	36.8	0.14	{0.00}	>1e6	13.9086	1.17	0.05694	1.61	489	36	454	7	448	5
AR23a rest	n5699@15	478.2	74.7	37.7	0.15	{0.00}	>1e6	13.9857	1.23	0.05472	1.08	401	24	438	6	445	5
AR23a rest	n5699@10	989.9	98.7	76.9	0.10	{0.00}	>1e6	13.9981	1.15	0.05546	0.71	431	16	443	5	445	5
AR23a rest	n5699@6b	394.1	59.7	31.0	0.15	{0.00}	>1e6	13.9996	1.18	0.05577	1.21	443	27	445	6	445	5
AR23a rest	n5699@16	666.3	77.6	51.9	0.11	{0.04}	44625	14.0109	1.22	0.05632	1.00	465	22	448	6	444	5
AR23a rest	n5699@5	499.4	73.5	39.3	0.15	{0.03}	63450	14.0312	1.18	0.05718	1.08	499	24	453	6	444	5
AR23a rest	n5699@4	345.4	51.8	27.2	0.15	{0.00}	>1e6	14.0445	1.22	0.05737	1.30	506	29	454	7	443	5
AR23a rest	n5699@17	478.9	68.2	37.4	0.14	{0.00}	>1e6	14.0590	1.18	0.05543	1.14	430	25	441	6	443	5
AR23a rest	n5699@2	356.3	51.5	27.9	0.14	{0.00}	>1e6	14.0719	1.22	0.05539	1.38	428	31	440	7	443	5
AR23a rest	n5699@25	478.6	74.0	37.5	0.15	{0.07}	28751	14.0738	1.19	0.05632	1.12	465	25	446	6	443	5
AR23a rest	n5699@17b	710.8	135.4	56.3	0.19	{0.02}	81741	14.0778	1.19	0.05618	0.93	460	21	445	5	442	5
AR23a rest	n5699@23b	453.9	48.4	34.9	0.10	{0.03}	66274	14.1172	1.22	0.05502	1.13	413	25	437	6	441	5
AR23a rest	n5699@12	586.8	62.4	45.2	0.11	{0.02}	103028	14.1224	1.21	0.05556	1.16	435	26	440	6	441	5
AR23a rest	n5699@19	506.6	57.2	39.0	0.10	{0.01}	198985	14.1257	1.20	0.05548	1.11	431	25	439	6	441	5
AR23a rest	n5699@24	426.0	63.6	33.2	0.15	{0.05}	34215	14.1328	1.24	0.05485	1.60	406	36	435	7	441	5
AR23a rest	n5699@20	336.2	42.9	26.0	0.12	{0.04}	46048	14.1370	1.28	0.05507	1.36	415	30	436	7	441	5
AR23a rest	n5699@9	704.2	73.6	54.2	0.11	{0.00}	>1e6	14.1394	1.16	0.05546	0.79	431	18	439	5	441	5
AR23a rest	n5699@6	329.3	43.7	25.5	0.13	{0.00}	>1e6	14.1498	1.20	0.05427	1.36	382	31	431	6	440	5
AR23a rest	n5699@1	499.8	46.5	38.3	0.09	{0.00}	>1e6	14.1681	1.16	0.05570	1.22	440	27	440	6	440	5
AR23a rest	n5699@26	393.1	65.2	30.7	0.16	1.47	1270	14.1897	1.41	0.05741	3.05	507	67	450	12	439	6
AR23a rest	n5699@1c	603.8	87.0	46.8	0.14	{0.00}	>1e6	14.1902	1.18	0.05581	1.00	445	22	440	6	439	5
AR23a rest	n5699@21	298.0	34.3	22.9	0.11	{0.00}	>1e6	14.2138	1.21	0.05586	1.41	447	31	440	7	438	5
AR23a rest	n5699@13	327.5	38.5	25.1	0.11	{0.00}	>1e6	14.2417	1.24	0.05556	1.54	435	34	437	7	437	5

AR23a rest	n5699@7	577.6	108.8	45.2	0.19	{0.02}	83432	14.2492	1.26	0.05593	0.82	450	18	439	5	437	5
AR23a rest	n5699@22b	500.3	70.9	38.5	0.13	{0.01}	261914	14.2523	1.27	0.05568	1.11	439	25	438	6	437	5
AR23a rest	n5699@18	329.4	52.8	25.5	0.15	{0.06}	32043	14.2592	1.27	0.05604	1.39	454	31	440	7	437	5
AR23a rest	n5699@8	287.1	26.2	21.8	0.10	{0.04}	51167	14.2953	1.30	0.05524	1.49	422	33	434	7	436	5
AR23a rest	n5699@9b	462.9	67.1	35.6	0.15	{0.00}	>1e6	14.3267	1.24	0.05554	0.96	434	21	435	6	435	5
AR23a rest	n5699@26b	281.3	25.0	21.0	0.09	0.28	6705	14.4995	1.28	0.05539	1.86	428	41	430	8	430	5

Table S3. U-Pb TIMS data for titanite

Sample name	Nr.	Properties	Weight [µg] (1)	U [ppm] (1)	Th/U (3)	Pbc [ppm] (1,2)	Pbcom [pg] (4)	$^{206}Pb/^{204}Pb$ (5)	$^{207}Pb/^{235}U$ (6)	2σ [abs] (6)	$^{206}Pb/^{238}Pb$ (6)	2σ [abs] (6)	ρ (6)	$^{206}Pb/^{238}U$ [Ma] (6)	2σ [Ma] (6)	$^{207}Pb/^{235}U$ [Ma] (6)	2σ [Ma] (6)
A01	502/17	brown grain	31	93	3.48	0.74	28.1	459	0.5478	0.0082	0.0707	0.00067	0.69	440.2	4.0	443.6	5.4
A01	502/S.65	euhedral brown grain	35	201	1.98	1.76	63.7	499	0.5340	0.0038	0.0695	0.00016	0.40	432.9	1.0	434.5	2.5
A01	502/16	euhedral brown grain	37	158	1.95	1.03	42.9	594	0.5337	0.0042	0.0692	0.00027	0.57	431.4	1.6	434.2	2.8
A01	507/S.67	brown fragment	77	108	2.57	1.33	104.0	366	0.5325	0.0050	0.0695	0.00018	0.33	433.4	1.1	433.4	3.3
A01	507/S.69	brown fragment	67	76	3.21	0.99	68.0	342	0.5295	0.0052	0.0693	0.00017	0.30	431.9	1.0	431.5	3.5
A01	502/18	big brown fragment	84	223	1.33	1.33	114.6	702	0.5241	0.0037	0.0687	0.00019	0.55	428.1	1.2	427.9	2.4
UL248	502/22	pale brown	17	45	5.65	3.58	65.0	68	0.5580	0.0369	0.0700	0.00059	0.27	436.4	3.6	450.3	23.8
UL248	502/23	brown, round	19	73	0.05	2.68	55.4	124	0.5243	0.0138	0.0692	0.00027	0.13	431.1	1.6	428.0	9.2
UL248	502/24	flat, pale brown	17	27	0.08	2.31	44.0	62	0.5386	0.0323	0.0693	0.00054	0.08	431.6	3.3	437.5	21.1

(1) weight and concentrations are known to better than 10%

(2) Pbc = initial common Pb, corrected for fractionation and blank

(3) model Th/U calculated from 206Pb/208Pb ratio and age of sample

(4) Pbcom = total common Pb in sample (initial + blank)

(5) raw data corrected for fractionation

(6) corrected for fractionation, spike, blank and initial common Pb